land

MDPI

Article

Spatial Heterogeneity of Land-Surface Energy-Balance Trends Across an Arid Coastal–Mountain Gradient: Multi-Variable MODIS Evidence of Spatially Uneven Dryland Recovery in Jizan, Saudi Arabia (2003–2023)

Islam M. Hamdi [1,*], Katarzyna Kubiak-Wójcicka [2,*], Amnah Aldohan [3], Martina Zeleňáková [4], Shouq Al-Absi [5], Jumah I. Ain [6] and Youssef M. Youssef [7]

[1] Department of Geography and GIS, Faculty of Arts, Beni-Suef University, Beni-Suef 62521, Egypt
[2] Department of Hydrology, Cryology and Water Management, Faculty of Earth Sciences and Spatial Management, Nicolaus Copernicus University, 87-100 Toruń, Poland
[3] Department of Geography and Environmental Sustainability, College of Humanities and Social Sciences, Princess Nourah bint Abdulrahman University, P.O. Box 84428, Riyadh 11671, Saudi Arabia; aaalasgah@pnu.edu.sa
[4] Faculty of Civil Engineering, Technical University of Košice, 04200 Košice, Slovakia; martina.zelenakova@tuke.sk
[5] Department of Physical Sciences–Geographic Information Systems (GIS) Program, Faculty of Science, University of Jeddah, Jeddah, Saudi Arabia; smalabsi@uj.edu.sa
[6] Geography Department, College of Humanities and Social Sciences, King Saud University, Riyadh 12372, Saudi Arabia; jain@ksu.edu.sa
[7] Geological and Geophysical Engineering Department, Faculty of Petroleum and Mining Engineering, Suez University, Suez 43518, Egypt; youssef.ibrahim@pme.suezuni.edu.eg
* Correspondence: islammohamed@art.bsu.edu.eg (I.M.H.); kubiak@umk.pl (K.K.-W.)

Abstract

Dryland systems are commonly assumed to degrade through the Charney–Otterman feedback, in which vegetation loss raises surface albedo, cools the atmospheric column, suppresses rainfall and drives further vegetation loss. Satellite evidence of dryland greening and of strong intra-regional heterogeneity now questions whether this pathway can be presumed at the sub-national scales at which land management is delivered. This study examines whether the land-surface signature associated with this feedback (daytime warming, vegetation decline and surface brightening) is present across the seventeen governorates of the Jizan region, southwestern Saudi Arabia, a hyper-arid to semi-arid transect that passes from coastal sabkha through irrigated plains to terraced highlands within 80 km. Daytime and nighttime land surface temperature (LST), NDVI and shortwave black-sky albedo from MODIS were analysed for 2003–2023 using Theil–Sen slopes and Mann–Kendall tests with autocorrelation correction and false-discovery-rate control, bivariate tercile classification, pixel-level correlation under three metrics, and principal component analysis combined with Ward clustering. Nighttime LST rose significantly in 16 of 17 governorates (+0.030 to +0.077 °C yr^{-1}), whereas no governorate warmed significantly by day and five cooled significantly (−0.029 to −0.099 °C yr^{-1}; two after adjustment). NDVI increased significantly in all 17 governorates (marginally in Farasan) and albedo declined significantly in twelve (seven after adjustment). Two principal components explained 93.6% of the trend variance, and Ward clustering resolved four regimes; under block-bootstrap resampling the highland–lowland division was the most stable feature of this partition, and the four regimes are therefore read as gradations in recovery strength rather than as sharply separated classes. No governorate displayed the absolute degradation signature. The regime closest to it in relative terms, formed by Ad Darb, Ar Rayth, Farasan and Jizan, combined the weakest greening with near-stable daytime LST and albedo, which indicates lagging rather

Check for updates

Academic Editors: Deirdre Dragovich, Imane Serbouti and Mustapha Hakdaoui

Received: 24 September 2026
Revised: 6 November 2026
Accepted: 16 November 2026
Published: 18 November 2026

Copyright: © 2026 by the authors. Licensee MDPI, Basel, Switzerland. This article is an open access article distributed under the terms and conditions of the Creative Commons Attribution (CC BY) license.

than reversed recovery. Elsewhere, the land surface is evolving in a recovery-consistent direction consistent with a change in surface properties rather than with radiative feedback alone; the roles of irrigation, soil moisture and land-cover change in this evolution remain to be established with independent data. The framework offers a transferable, satellite-only diagnostic for targeting restoration and land-degradation-neutrality efforts in dryland administrative units.

Keywords: dryland systems; land degradation; land surface temperature; NDVI; surface albedo; Charney–Otterman feedback; MODIS; Arabian Peninsula

1. Introduction

Drylands occupy roughly 41% of the terrestrial surface and support close to 38% of the global population, which places them at the centre of contemporary concerns about land degradation, water security, agricultural sustainability and ecosystem resilience [1,2]. These systems respond to global change through the combined pressures of climate variability, agricultural intensification, urban growth and groundwater over-abstraction, and their trajectories increasingly diverge between degradation and recovery. Desertification remains the most extensively documented of these trajectories [3,4]. Its theoretical foundation is the Charney–Otterman hypothesis, which proposes that vegetation removal raises surface albedo, reduces net radiative heating of the atmospheric column, suppresses convective activity and precipitation, and thereby closes a self-reinforcing loop between vegetation loss, altered surface energy exchange and progressive land degradation [5,6]. The daytime surface-temperature response is not fixed by this mechanism: brightening alone reduces absorbed shortwave radiation and tends to cool the surface [5], whereas the loss of evapotranspiration that accompanies vegetation removal tends to warm it, so that the thermal signature of degradation depends on which pathway dominates [7]. For several decades this mechanism has framed the study of climate–land surface interactions in arid and semi-arid environments [7].

The satellite record assembled since the 1980s has shown that dryland responses are considerably more heterogeneous than the hypothesis anticipates. Rather than exhibiting widespread decline, many dryland regions have greened [8–11], with the most pronounced gains concentrated in intensively managed landscapes where restoration programmes, irrigation development and afforestation have raised ecosystem productivity [12]. Dryland trajectories therefore cannot be reduced to a single degradation pathway. Spatial heterogeneity has become a defining property of contemporary dryland dynamics, and distinguishing degradation from recovery and from transitional states requires multi-variable monitoring at the administrative scales at which land-management decisions are taken and evaluated [2]. Because regional and national aggregates can conceal opposing signals within a single jurisdiction [13,14], the resilience of a dryland system is best assessed where its management is delivered.

Observations from the Moderate Resolution Imaging Spectroradiometer (MODIS) sensors aboard the Terra and Aqua satellites have provided a consistent multi-decadal record of the land surface since the early 2000s [15]. Among the available products, three variables carry particular diagnostic weight for dryland surface-energy-balance monitoring. Land surface temperature (LST), retrieved with generalised split-window algorithms, is available as separate daytime and nighttime fields that sample distinct components of the surface energy budget [16,17]. The Normalised Difference Vegetation Index (NDVI) provides a standard proxy for canopy greenness and photosynthetic activity [18–21]. Broadband shortwave albedo, derived from kernel-driven inversions of the bidirectional reflectance dis-

tribution function, quantifies the hemispherical reflectance on which the Charney–Otterman feedback depends [22–24]. Taken together, the NDVI–LST–albedo triplet has become the canonical combination for diagnosing dryland degradation and recovery [7,25–27]: the negative pixel-level association between NDVI and LST is exploited for drought monitoring [28], whereas the positive coupling between LST and albedo and the inverse NDVI–albedo relationship give direct empirical access to the energy-balance pathways of the feedback [29,30]. Robust trend detection in such series rests on non-parametric estimators, notably the Theil–Sen slope and the Mann–Kendall test with variance correction for serial autocorrelation [31–35]. The global documentation of asymmetric warming, in which nocturnal warming outpaces daytime warming because of changes in soil moisture, vegetation and cloud cover [36–39], has additionally established daytime and nighttime LST as complementary diagnostics that should be retained separately rather than averaged [40–42].

The Arabian Peninsula ranks among the most climate-sensitive regions of the world, with warming rates exceeding the global mean and marked changes in precipitation regimes [43–45]. Station-based analyses for Saudi Arabia indicate significant increases in annual maximum, mean and minimum temperatures at rates near 0.71, 0.60 and 0.48 °C per decade [45], accompanied by rising frequencies of warm days and warm nights and a decline in cold extremes [46–48]. Annual precipitation has decreased over recent decades, escalating drought risk and water-resource vulnerability in a region already dependent on non-renewable groundwater [49,50]. Remote sensing studies have begun to document the environmental consequences of these pressures, reporting MODIS-derived warming across the Red Sea mountain ranges [51] and localised greening associated with irrigated agricultural development in several parts of the Kingdom [52].

Important gaps nevertheless remain in the monitoring of surface-energy-balance change in Saudi Arabia. Most regional studies have treated LST or NDVI in isolation, or have analysed national-scale aggregates that conceal the sub-regional heterogeneity now recognised globally [46,49,51,52]. The diurnal asymmetry of LST trends, which at global and continental scales separates surface-property change from radiative forcing, has received only fragmentary attention on the Peninsula [13,37–39,53]. Integrated NDVI–LST analyses and multivariate clustering have been applied in other arid environments [7,25], but their combined implementation within a governorate-level framework remains rare. The parallel use of Pearson, Spearman and Kendall coefficients to secure inferential robustness under the non-Gaussian, outlier-prone conditions typical of dryland surface variables is likewise uncommon in the regional literature [54].

The Jizan region in southwestern Saudi Arabia, on the Red Sea coast, is a particularly instructive setting for these questions. Within a horizontal distance of less than 80 km it encompasses the hyper-arid Tihama coastal plain, a semi-arid foothill transition and the Sarawat Mountains, whose upper slopes receive seasonal moisture linked to Indian Ocean monsoonal circulation [55]. This steep environmental gradient coincides with rapid agricultural expansion, growing groundwater-fed irrigation, urban growth around Jizan City, long-established terraced cultivation on the escarpment and strong maritime influence, so that degradation and recovery processes operate side by side [56–58]. No governorate-scale assessment integrating several surface-energy-balance indicators has yet been undertaken for the region, despite its environmental and socio-economic importance.

The present study addresses these gaps through an integrated analysis of MODIS-derived daytime LST, nighttime LST, NDVI and broadband shortwave black-sky albedo across the seventeen governorates of Jizan for 2003–2023. Non-parametric Theil–Sen slopes and Mann–Kendall significance are estimated, in both original and autocorrelation-corrected form, for each variable and governorate. The spatial co-evolution of the four variables is mapped through a bivariate tercile classification of all physically meaningful variable pairs. Pixel-level co-variation is quantified with three correlation metrics in parallel, and the multivariate trend structure is characterised through unsupervised principal component analysis and Ward hierarchical clustering of the standardised governorate-level slope matrix. The combined framework is designed to test whether the land-surface signature associated with the Charney–Otterman feedback (rising daytime LST, declining NDVI and rising albedo; hereafter the Charney–Otterman-related surface signature) is present at the governorate scale, focusing on the land-surface expression of the feedback rather than on its atmospheric components (column radiative cooling, subsidence and rainfall suppression), to characterise the diurnal asymmetry of the regional thermal response, to identify spatially coherent trend regimes at the administrative scale and to provide a transferable, low-cost diagnostic that can support the targeting of restoration and land-degradation-neutrality measures under the environmental commitments of the Saudi Vision 2030 framework.

2. Materials and Methods

2.1. Study Area

The Jizan region occupies the southwestern extremity of Saudi Arabia along the Red Sea coast between approximately 16.3° N and 18.1° N and between 41.5° E and 43.4° E (Figure 1). It is subdivided into 17 governorates, whose boundaries were taken from the GADM 4.1 database (level 2) [59]. In this dataset the unit named Jizan is a multipart polygon that comprises the coastal area around Jizan City (about 185 km^2) and a larger inland block (about 845 km^2) north of Baysh, between Ad Darb and Ar Rayth (Figure 1); the statistics reported below for the Jizan unit therefore refer mainly to the inland block (Section 4.6). The region encompasses three physiographic zones that succeed one another over a horizontal distance of less than 80 km: the hyper-arid Tihama coastal plain (0–200 m a.s.l.), a semi-arid foothill transitional belt (200–800 m a.s.l.) and the western escarpment of the Sarawat highlands (800–2628 m a.s.l.). Under the Köppen–Geiger classification the region falls within the BWh category, with a mean annual air temperature near 30.6 °C and an aridity index between 0.03 and 0.20 [55]. The topographic and land-cover gradient, from bare coastal sabkha through irrigated agricultural plots to sparse montane scrub and terraced slopes, provides a natural laboratory in which the canonical land-degradation signature of warming, browning and brightening predicted by surface energy-balance theory can be tested against the recovery signature produced by land-use change [5–7,58].

2.2. Data Sources

Four satellite-derived surface variables were retrieved for the 21-year window 2003–2023 from the MODIS Collection 6.1 archive through the Google Earth Engine platform (Google LLC, Mountain View, CA, USA) [60], in which quality screening and seasonal compositing were performed before export.

2.2.1. Land Surface Temperature

Daytime LST (LST_{Day}; Terra overpass at about 10:30 local solar time) and nighttime LST (LST_{Night}; Terra overpass at about 22:30 local solar time) were obtained from the MODIS Terra MOD11A2 Collection 6.1 eight-day composite product at 1 km spatial resolution, as Band 1 and Band 2 respectively [16,17,61]. Both fields were retained because they capture distinct components of the surface energy balance. LST_{Day} is governed by absorbed shortwave radiation and by the partitioning of available energy between sensible and latent heat, and therefore integrates the radiative (albedo) and evaporative pathways through which vegetation change acts on the surface energy balance [5,6], whereas LST_{Night} is governed primarily by surface thermal inertia and longwave emission and therefore serves as a complementary indicator of soil-moisture and surface-property change [30]. Only pixels with quality-control bits 0–1 equal to 00 (LST produced, good quality) or 01 (LST produced, other quality) were retained, and pixels for which no LST was produced (10 and 11) were discarded before seasonal aggregation. Each seasonal composite is the mean of all retained 8-day values within the season.

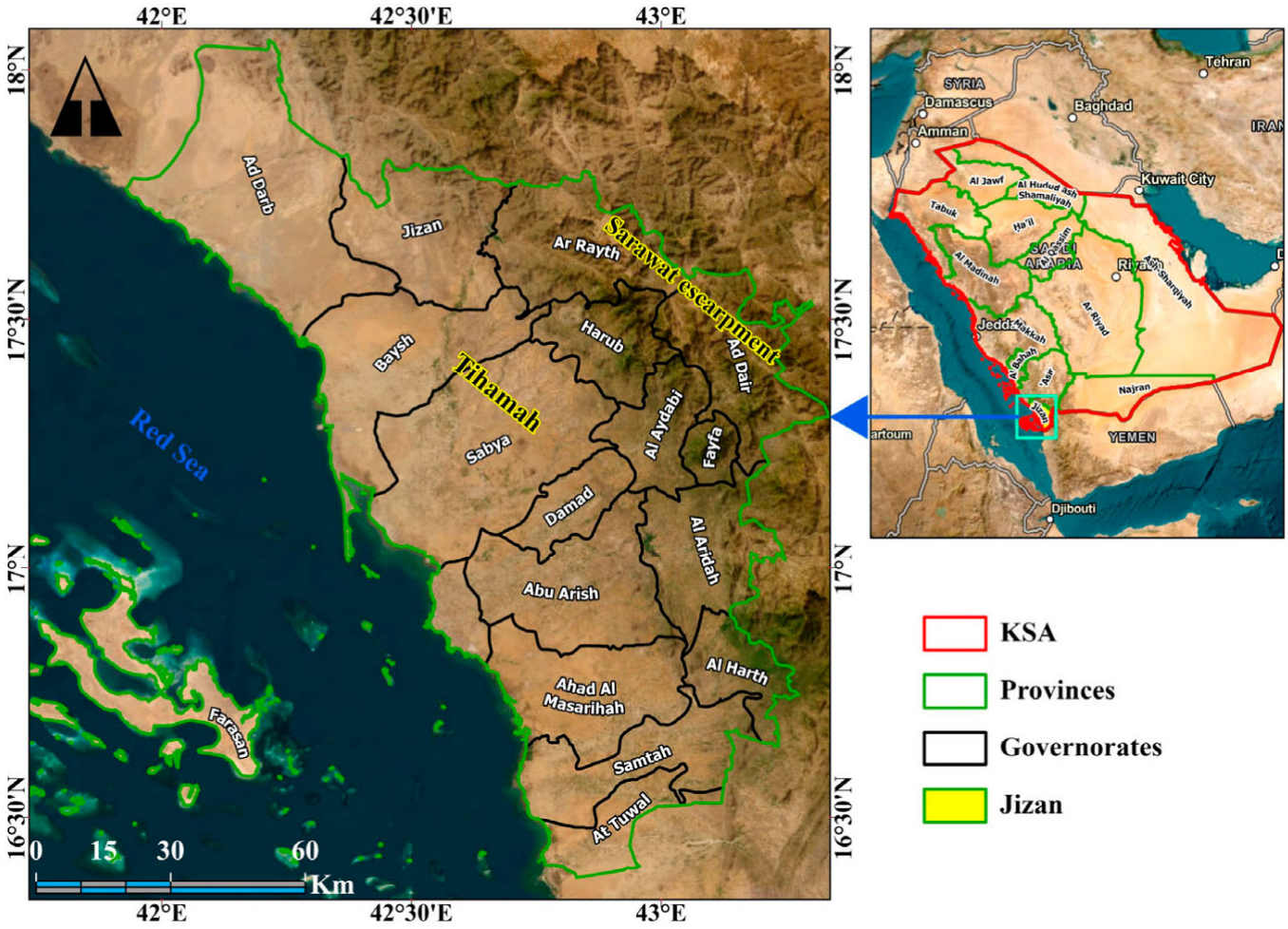


Figure 1. Location of the Jizan region in southwestern Saudi Arabia and its seventeen governorates (GADM 4.1, level 2), shown on satellite base imagery, with the Red Sea, the Tihama coastal plain and the Sarawat escarpment labelled. The polygon labelled Jizan, north of Baysh, is the inland block of the multipart Jizan unit (Section 2.1). The inset shows the position of the region among the provinces of the Kingdom of Saudi Arabia. The black arrow at the top left of the main map is the north arrow; the bar scale is in kilometres.

2.2.2. Normalised Difference Vegetation Index (NDVI)

NDVI was retrieved from the MODIS Terra MOD13A2 Collection 6.1 sixteen-day composite product at 1 km spatial resolution [20]. The MOD13A2 algorithm selects the best-quality pixel within each sixteen-day window on the basis of low cloud cover, low view angle and highest NDVI value; its pixel-reliability summary layer (SummaryQA) was used to retain only pixels classed as good (0) or marginal (1) and to exclude snow/ice (2), cloudy (3) and fill pixels; each seasonal composite is the mean of the retained 16-day values within the season. NDVI is defined as

$$\mathrm{NDVI} = \frac{\rho_{\mathrm{NIR}} - \rho_{\mathrm{Red}}}{\rho_{\mathrm{NIR}} + \rho_{\mathrm{Red}}}, \quad (1)$$

where ρ_{NIR} and ρ_{Red} are the bidirectional surface reflectances centred at 858 nm and 645 nm respectively [18,19]. NDVI ranges from −1 to +1, and values above about 0.20 are usually interpreted as vegetated cover in Saudi Arabia [52].

2.2.3. Surface Albedo

Shortwave broadband black-sky albedo (directional-hemispherical reflectance at local solar noon, 0.3–5.0 µm) was obtained from the MODIS Terra and Aqua MCD43A3 Collection 6.1 daily product, whose native resolution is 500 m [23,24]. MCD43A3 is generated daily from a sixteen-day moving retrieval window centred on the day of interest, combining observations from both platforms to maximise the probability of high-quality kernel-driven BRDF inversions [22]. Only full-inversion retrievals (mandatory quality-assurance band equal to 0) were retained, and each seasonal composite is the mean of the retained daily values within the season. Black-sky albedo depends on the solar zenith angle, but because the analysis compares the same calendar seasons across years, the local-noon illumination geometry of a given pixel is the same in every year and cannot by itself generate a trend. The white-sky (bihemispherical) albedo, which is independent of illumination geometry, was used as a sensitivity check: its governorate-level slopes differ from the black-sky slopes by less than 10% in magnitude (the two fields differ by about 0.013 in level), the same twelve governorates show significant declines, and the cluster partition of Section 3.3 is identical (Section 4.6).

2.2.4. Temporal Aggregation

For each calendar year y and each variable V, the sub-annual composites were first aggregated into four seasonal means following the standard climatological calendar:

$$\overline{V}_{s,y} = \frac{1}{N_{s,y}} \sum_{t \in s} V_t(x), s \in \{\mathrm{DJF}, \mathrm{MAM}, \mathrm{JJA}, \mathrm{SON}\}, \quad (2)$$

where V denotes any of the four variables, t indexes the valid sub-annual composites falling within season s of year y, and $N_{s,y}$ is the number of valid composites. Annual means were then computed as the arithmetic average of the four seasonal fields:

$$\overline{V}_y(x) = \frac{1}{4} \sum_{s} \overline{V}_{s,y}(x). \quad (3)$$

All subsequent analyses, comprising trend estimation, bivariate classification, pixel-level correlation and multivariate clustering, were performed on the annual fields $V_y(x)$ rather than on individual seasonal composites, so as to suppress the strong seasonal cycle that would otherwise dominate the inter-variable signal.

Equal weighting of the four seasons was chosen deliberately. Within each season, the seasonal composite is the mean of all quality-screened observations available in that season (8-day LST values, 16-day NDVI values or daily albedo retrievals), so that within-season

gaps are absorbed at the compositing stage. A mean of all observations in a year, weighted by their number, would give greater weight to the clearest season at each pixel and would yield an annual index whose seasonal composition varied between pixels and between years. The seasonally balanced mean of Equation (3) avoids this, at the cost of giving a sparsely sampled season the same weight as a well-sampled one. Where a seasonal mean was undefined at a pixel, the annual value was computed from the remaining seasons. Such pixel-years were rare: 0.02% of the pixel-years within the governorate polygons for LST, 0.09% for albedo and 0.9% for NDVI, almost all of them coastal mixed land–water pixels (9.7% of the pixel-years in Farasan, 1.3% in Baysh and 1.1% in the Jizan unit; none in the highland governorates). Recomputing the governorate series with these pixel-years excluded changed no slope by more than 0.0003 °C yr^{-1} (LST) or 3×10^{-5} yr^{-1} (NDVI and albedo) and altered no significance decision except the marginal NDVI trend of Farasan ($p = 0.050$ to 0.065); the cluster partition of Section 3.3 was unchanged. Because the trend analysis is carried out on each governorate's own annual series, a seasonal sampling imbalance that is constant through time alters the level of the series but not its Theil–Sen slope, so that only a change in seasonal coverage over the study period could bias the trends. The proportion of pixel-years with incomplete seasonal coverage showed no significant trend over 2003–2023 for any variable (Mann–Kendall $p \geq 0.16$).

The three products also differ in platform, compositing period and observation time. LST and NDVI are Terra products (8-day and 16-day composites, respectively), whereas MCD43A3 combines Terra and Aqua observations within a 16-day moving window to retrieve a daily albedo [23,24]. These differences were reconciled at the temporal scale of the analysis rather than composite by composite: each product was averaged to the same calendar seasons and years (Equations (2) and (3)), composites being assigned to seasons by their start date, so that every variable enters the analysis as a seasonally balanced annual mean for an identical set of 21 years. Because the MCD43A3 albedo is a property of the BRDF model fitted to the 16-day window, the inclusion of Aqua observations increases the angular sampling of the inversion, and the black-sky albedo is evaluated at local solar noon for every pixel irrespective of the overpass time of either platform. Consecutive daily retrievals share most of their input observations; the seasonal mean of the daily values is therefore a smoothed estimate rather than an average of independent samples.

2.3. Pre-Processing and Spatial Harmonisation

All products were exported on a common geographic grid (EPSG:4326) with a pixel size of 0.00898° (about 1 km at the latitude of Jizan), which corresponds to the native resolution of MOD11A2 and MOD13A2; the 500 m MCD43A3 albedo was resampled to this grid at export using the default nearest-neighbour sampling of the export tool. Every analysis pixel therefore refers to the same footprint for all four variables, and no further resampling was applied. All seasonal rasters were clipped to the Jizan administrative boundary with the rasterio library [62] (rasterio.mask.mask with crop enabled) after reprojecting each boundary geometry to the raster coordinate reference system. Pixel values outside physically plausible ranges were masked as invalid using the following thresholds: LST_{Day}, −10 °C to 70 °C; LST_{Night}, −10 °C to 50 °C; NDVI, −0.30 to 1.00; shortwave black-sky albedo, 0.00 to 0.70.

Governorate membership and pixel validity were handled as follows. Pixels were assigned to a governorate when their centre fell inside the governorate polygon (the default all_touched = False option of rasterio.features.geometry_mask), so that each boundary pixel belongs to exactly one governorate and no pixel is counted twice. Pixel validity was defined at two levels. For the governorate series (Section 2.4), a pixel-year entered the zonal mean of a variable whenever that variable was valid, irrespective of the other variables. For

the bivariate classification (Section 2.6) and the pixel-level correlations (Section 2.7), only pixels valid for both variables of a pair were used; this is why pixel counts differ slightly between pairs for the same governorate (for example, 671 pixels for Farasan in the pairs involving LST and 727 in the NDVI × Albedo pair). Coastal mixed pixels for which no LST was retrieved were thereby excluded from all LST-based pairs.

2.4. Zonal Aggregation

For each governorate g with administrative polygon G_g, the annual zonal mean of each variable was computed as

$$\overline{V}_{g,y} = \frac{1}{|P_g|} \sum_{x \in P_g} \overline{V}_y(x), \tag{4}$$

where P_g is the set of pixels whose centres fall within G_g and for which the variable is valid, and $|P_g|$ is its cardinality. Years for which no valid pixel existed within a governorate were treated as missing; this situation did not arise, and all 68 governorate series are complete ($n = 21$). The zonal statistic is the standard unit of analysis in administrative-scale land-degradation assessments and aligns the results with the units through which regional land policy is designed and delivered [3,7,63].

2.5. Non-Parametric Trend Estimation

The temporal trend of each governorate-level annual series was estimated with the Theil–Sen median slope estimator [31,32], which has a 29.3% breakdown point against outliers [64] and does not require Gaussian residuals. For a series of n paired (year, value) observations (t_i, y_i), the Theil–Sen slope is

$$\hat{\beta}_{TS} = \text{median}\left\{\frac{y_j - y_i}{t_j - t_i} : 1 \le i < j \le n\right\}. \tag{5}$$

Statistical significance was assessed with the Mann–Kendall (MK) rank-based test [33,34]. The MK statistic S is

$$S = \sum_{i=1}^{n-1} \sum_{j=i+1}^{n} \text{sgn}(y_j - y_i), \tag{6}$$

with a tie-corrected variance

$$\text{Var}(S) = \frac{n(n-1)(2n+5) - \sum_p t_p\left(t_p - 1\right)\left(2t_p + 5\right)}{18}, \tag{7}$$

where t_p is the number of tied values in the p-th tie group. The standardised test statistic is

$$Z = \begin{cases} \frac{S-1}{\sqrt{\text{Var}(S)}}, & S > 0, \\ 0, & S = 0, \\ \frac{S+1}{\sqrt{\text{Var}(S)}}, & S < 0, \end{cases} \tag{8}$$

and a trend is declared statistically significant at the 95% confidence level when $|Z| > 1.96$ ($p < 0.05$). The variance correction for serial autocorrelation [35],

$$\text{Var}^*(S) = \text{Var}(S) \cdot \frac{n}{n_e^*}, \tag{9}$$

was also computed, where n^*_e is the effective sample size. Following Hamed and Rao [35], as implemented in the hamed_rao_modification_test function of the pymannkendall package [65] (version 1.4.3), each series was detrended with its Theil–Sen slope and converted to ranks; the lag-k autocorrelation coefficients r_k of these ranks were computed for all lags $k = 1, \ldots, n-1$, and only coefficients lying outside the 95% confidence band ($|r_k| > 1.96/\sqrt{n}$)

were retained, which is the truncation rule of the method. The variance-inflation factor is then $n/n^*_e = 1 + 2[n(n-1)(n-2)]^{-1} \Sigma\,(n-k)(n-k-1)(n-k-2)r_k$, the sum running over the retained lags. With $n = 21$, negative autocorrelation estimates can produce factors below 1, which would make the corrected test more liberal than the original one; because such estimates are unstable in short series, the factor was bounded below at 1, so that the correction can only make the test more conservative. Factors above 1 were applied as computed; the smallest effective sample size obtained in this way was 8.5 (albedo series), and no further adjustment was made. Both the original and the modified results are reported for every governorate and variable (Appendix A, Tables A1 and A2), and cases in which the two formulations disagree are flagged. Trends were computed with the pymannkendall package [65], with the bounded correction factor applied as described above.

Because the same test was applied to 17 governorates for each of four variables, the probability of false positives increases with the number of tests [66,67]. The false discovery rate (FDR) was therefore controlled with the Benjamini–Hochberg procedure [66], applied separately to the 17 governorate-level tests of each variable, which is the family relevant to statements of the form "significant in x of 17 governorates". Adjusted values (q) are reported alongside the unadjusted p-values, and a trend is described as significant after adjustment when $q < 0.05$. Applying the procedure jointly to all 68 tests was less conservative for LST_{Day} and albedo (five and nine significant trends, respectively, instead of two and seven) and did not change the results for LST_{Night} and NDVI; the per-variable results are therefore used throughout.

2.6. Bivariate Tercile Classification

To examine whether the components of the Charney–Otterman-related surface signature and its nighttime analogue co-occur at the pixel level, a bivariate tercile classification was applied to five physically meaningful variable pairs: LST_{Day} × NDVI, LST_{Day} × Albedo, LST_{Night} × NDVI, LST_{Night} × Albedo and NDVI × Albedo. The daytime pairs, together with NDVI × Albedo, target the land-surface components of the Charney–Otterman loop; the two nighttime pairs extend the framework to nocturnal conditions and provide a complementary diagnostic of thermal-inertia and longwave-emission responses to land-surface modification.

For each variable V, two tercile thresholds $Q_{33}(V)$ and $Q_{67}(V)$ were estimated once from the pooled distribution of all valid pixels across the 21 annual fields of the Jizan domain. The use of pooled rather than year-specific thresholds is methodologically essential. Year-specific terciles would by construction partition each annual field into three approximately equal-area classes and would mask precisely the inter-annual variability the analysis is designed to reveal, whereas pooled thresholds provide a fixed long-term reference distribution against which each year's spatial configuration can be assessed. Because the thresholds of each variable were derived from all pixel-years in which that variable was valid, the same pair of thresholds applies in every variable pair in which the variable appears; a pixel-year was classified only when both variables of the pair were valid. The resulting classes describe the relative position of a pixel within the 2003–2023 distribution of the Jizan region; they are not ecologically validated degradation categories, and a pixel in the H class of albedo, for example, is bright relative to the region rather than degraded in an absolute sense.

Each pixel x in each annual field was then assigned to one of three classes for each variable:

$$\mathrm{Class}(V,x,y) = \begin{cases} \mathrm{L}, & \overline{V}_y(x) \le Q_{33}(V), \\ \mathrm{M}, & Q_{33}(V) < \overline{V}_y(x) \le Q_{67}(V), \\ \mathrm{H}, & \overline{V}_y(x) > Q_{67}(V). \end{cases} \quad (10)$$

The bivariate joint class for a variable pair (V_1, V_2) at pixel x in year y is the ordered pair of the two single-variable classes, which yields nine joint categories (LL, LM, LH, ML, MM, MH, HL, HM and HH), each mapped to a unique colour in a bivariate choropleth [68]. The classification was applied to each annual field independently, producing a 21-panel temporal sequence (2003–2023) for each of the five variable pairs that captures both the long-term spatial structure and the inter-annual reorganisation of the joint distribution.

2.7. Pixel-Level Correlation Analysis

To quantify the strength and direction of pixel-level co-variation among the four variables, three correlation coefficients were computed for each of the five variable pairs across the 17 governorates. For each governorate, all pixels valid for both variables of the pair in the two 21-year mean fields were extracted and the following metrics were evaluated. Pearson's product-moment coefficient r measures the linear association between two continuous variables [69]:

$$r_{XY} = \frac{\sum_{i=1}^{n}(X_i - \overline{X})(Y_i - \overline{Y})}{\sqrt{\sum_{i=1}^{n}(X_i - \overline{X})^2 \sum_{i=1}^{n}(Y_i - \overline{Y})^2}}. \quad (11)$$

Spearman's rank coefficient ρ_s measures the monotonic association between two variables without assuming linearity and was computed as Pearson's coefficient between the ranks of the two variables, tied values receiving their average (mid-)rank [70]:

$$\rho_s = \frac{\sum_{i=1}^{n}(R_i - \overline{R})(S_i - \overline{S})}{\sqrt{\sum_{i=1}^{n}(R_i - \overline{R})^2 \sum_{i=1}^{n}(S_i - \overline{S})^2}}, \quad (12)$$

where R_i and S_i are the (mid-)ranks of X_i and Y_i and $\overline{R}$ and $\overline{S}$ are their means; in the absence of ties this expression reduces to the familiar form $1 - 6\Sigma d_i^2/[n(n^2-1)]$, with $d_i = R_i - S_i$. Kendall's rank coefficient was computed in its tie-corrected form, τ_b [34], which provides a robust non-parametric measure of ordinal association with lower sensitivity to outliers than either Pearson's r or Spearman's ρ_s [71]:

$$\tau_b = \frac{n_c - n_d}{\sqrt{(n_0 - n_1)(n_0 - n_2)}}, \quad (13)$$

where n_c is the number of concordant pairs and n_d the number of discordant pairs among all pairwise comparisons, $n_0 = n(n-1)/2$, and $n_1 = \Sigma t_i(t_i - 1)/2$ and $n_2 = \Sigma u_j(u_j - 1)/2$ correct for groups of t_i tied values of X and u_j tied values of Y. Ties are relevant because the MODIS products are quantised (LST in steps of 0.02 K, NDVI in steps of 10^{-4} and albedo in steps of 10^{-3}), although averaging over 21 years makes exact ties in the mean fields rare. The parallel use of the three metrics reflects the fact that Pearson's r and Spearman's ρ_s can diverge substantially in the presence of non-linearity, outliers or non-Gaussian marginal distributions, whereas Kendall's τ_b yields the most conservative and distributionally robust estimate [54]. Results were visualised as hexagonal-bin density scatter plots, which avoid the over-plotting that affects conventional scatter plots when many points overlap [72]. The pixel-level coefficients are used descriptively, as measures of the strength and direction of spatial co-variation within each governorate. Neighbouring 1 km pixels share land cover, topography and climate and are therefore spatially autocorrelated, so the nominal pixel

count overstates the number of independent observations and p-values computed from it would overstate significance [73,74]. No inferential significance is therefore attached to individual coefficients, and their magnitudes are interpreted mainly where the three metrics agree in sign. The coefficients describe co-variation across space within a governorate; they are not evidence about the processes that generate the governorate-level temporal trends of Section 2.5, which address a different statistical question.

2.8. Multivariate Trend Characterisation Through PCA and Hierarchical Clustering

To synthesise the multivariate trend structure of the four variables across the 17 governorates without imposing pre-defined thresholds or directional rules, an unsupervised approach combining principal component analysis (PCA) and Ward hierarchical clustering was adopted. This approach is well established in regional climatology and pedoclimatic regionalisation [75,76] and is preferable to rule-based categorical classifications when the analytical aim is to let the multivariate structure of the data reveal its own groupings.

A feature matrix $\mathbf{F}$ of dimension 17 × 4 was constructed, in which each row g represents one governorate and each column v contains its Theil–Sen slope for one of the four variables $v \in \{\mathrm{LST_{Day}}, \mathrm{LST_{Night}}, \mathrm{NDVI}, \mathrm{Albedo}\}$. To ensure that all variables contribute equally despite their differing physical units and dynamic ranges, each column was standardised to zero mean and unit variance:

$$Z_{g,v} = \frac{F_{g,v} - \mu_v}{\sigma_v}, \tag{14}$$

where μ_v and σ_v are the mean and standard deviation (computed with divisor 17) of variable v across the 17 governorates. Principal component analysis was applied to the standardised matrix $\mathbf{Z}$ by singular value decomposition [77]:

$$\mathbf{Z} = \mathbf{U}\,\mathbf{S}\,\mathbf{V}^{\top}, \tag{15}$$

where the columns of $\mathbf{V}$ contain the variable loadings on each principal component and the product $\mathbf{US}$ contains the governorate scores in the orthonormal principal-component coordinate system. The explained variance ratio of the k-th principal component was computed as ${s_\mathrm{k}}^2/\Sigma_\mathrm{j}{s_\mathrm{j}}^2$, where s_k is the k-th singular value. The first two principal components were retained for biplot visualisation, in which the 17 governorates are positioned in PC1–PC2 space and the four variable loadings are overlaid as vector arrows indicating each variable's contribution to the two principal directions.

Hierarchical clustering was performed on the standardised feature matrix $\mathbf{Z}$ with Ward's minimum-variance linkage [76,78], which at each agglomerative step merges the two clusters whose union produces the smallest increase in the total within-cluster sum of squared Euclidean deviations. Ward linkage was chosen because it produces compact, similarly sized clusters that suit the relatively small sample size of $n = 17$. The optimal number of clusters k was determined with the silhouette coefficient [79], evaluated for $k = 2$–8. For each governorate i the silhouette coefficient is

$$\mathrm{Sil}(i) = \frac{b_i - a_i}{\max(a_i, b_i)}, \tag{16}$$

where a_i is the mean Euclidean distance from i to all other members of its own cluster and b_i is the minimum mean Euclidean distance from i to all members of any other cluster. The mean silhouette coefficient over the 17 governorates was computed for each candidate k, and the optimal k was the value that maximised it.

Because the feature matrix contains only 17 observations, the stability of the partition was examined in five ways. First, the mean silhouette value of each candidate solution was interpreted against the guideline of Kaufman and Rousseeuw [80], in which values

of 0.26–0.50 indicate a weak structure and values of 0.51–0.70 a reasonable one. Second, each governorate was removed in turn and the remaining 16 were re-standardised and re-clustered (leave-one-out). Third, the partition was recomputed with average and complete linkage and with *k*-means (100 random starts). Fourth, the standardisation of Equation (14) was replaced by a robust version based on the median and the scaled median absolute deviation, which limits the influence of outlying slopes. Fifth, uncertainty in the trend estimates was propagated by a moving-block bootstrap of each annual series (block length 3 years, 1000 replicates): the residuals around each Theil–Sen line were resampled in blocks, the slopes re-estimated, and the standardisation and clustering repeated. Agreement with the original partition was measured with the adjusted Rand index (ARI) [81], and the stability of individual clusters with the mean pairwise co-assignment frequency of their members across bootstrap replicates [82].

The clustering outputs were synthesised in a single composite figure comprising a PCA biplot of governorate positions in PC1–PC2 space coloured by cluster membership with variable loadings overlaid as arrows, a Ward dendrogram with branches coloured by terminal cluster assignment, a choropleth map of the Jizan governorates coloured by cluster assignment, and a cluster-signature heatmap displaying the mean standardised trend of each variable within each cluster. The heatmap summarises the relative trend profile of each cluster.

The cluster signatures in Table 1 list the variables whose mean standardised slope satisfies $|z| > 0.5$. This threshold corresponds to a departure of at least half a between-governorate standard deviation from the regional mean slope, a magnitude conventionally regarded as a medium standardised difference [83]; smaller departures are difficult to distinguish from the scatter of individual governorates around their cluster mean. Because any fixed threshold is partly arbitrary, the signatures were also examined for thresholds of 0.4, 0.6, 0.75 and 1.0 (Section 3.3). Since *z*-scores express each slope relative to the 17-governorate distribution, the signatures describe relative tendencies: a negative *z*-score for NDVI, for example, denotes greening slower than the regional mean, not a decline in NDVI. Cluster means of the absolute slopes in physical units are therefore reported alongside the *z*-scores (Section 3.3).

2.9. Software and Reproducibility

All analyses were implemented in Python 3.13 (Python Software Foundation, Wilmington, DE, USA). Raster input/output and clipping were handled with rasterio 1.5.2 [62], vector operations with geopandas 1.2.0 [84], numerical computation with NumPy 2.5.3 and SciPy 1.18.1 [85,86], non-parametric trend tests with pymannkendall 1.4.3 [65], Ward clustering and dendrogram construction with scipy.cluster.hierarchy [86], and figure production with matplotlib 3.11.2 [87]; silhouette values, adjusted Rand indices, and k-means partitions were computed with scikit-learn 1.9.1 [88], and the bounded Hamed–Rao correction, the Benjamini–Hochberg adjustment and the block bootstrap were implemented with NumPy and SciPy. Hexagonal-bin density scatter plots were generated with matplotlib.pyplot.hexbin using logarithmic colour normalization to resolve density structure in the tails of the pixel distributions. Principal component analysis was implemented directly through the NumPy singular-value decomposition routine so as to retain explicit control over the standardization step and the interpretation of the loading vectors. The complete workflow is summarised in Figure 2.

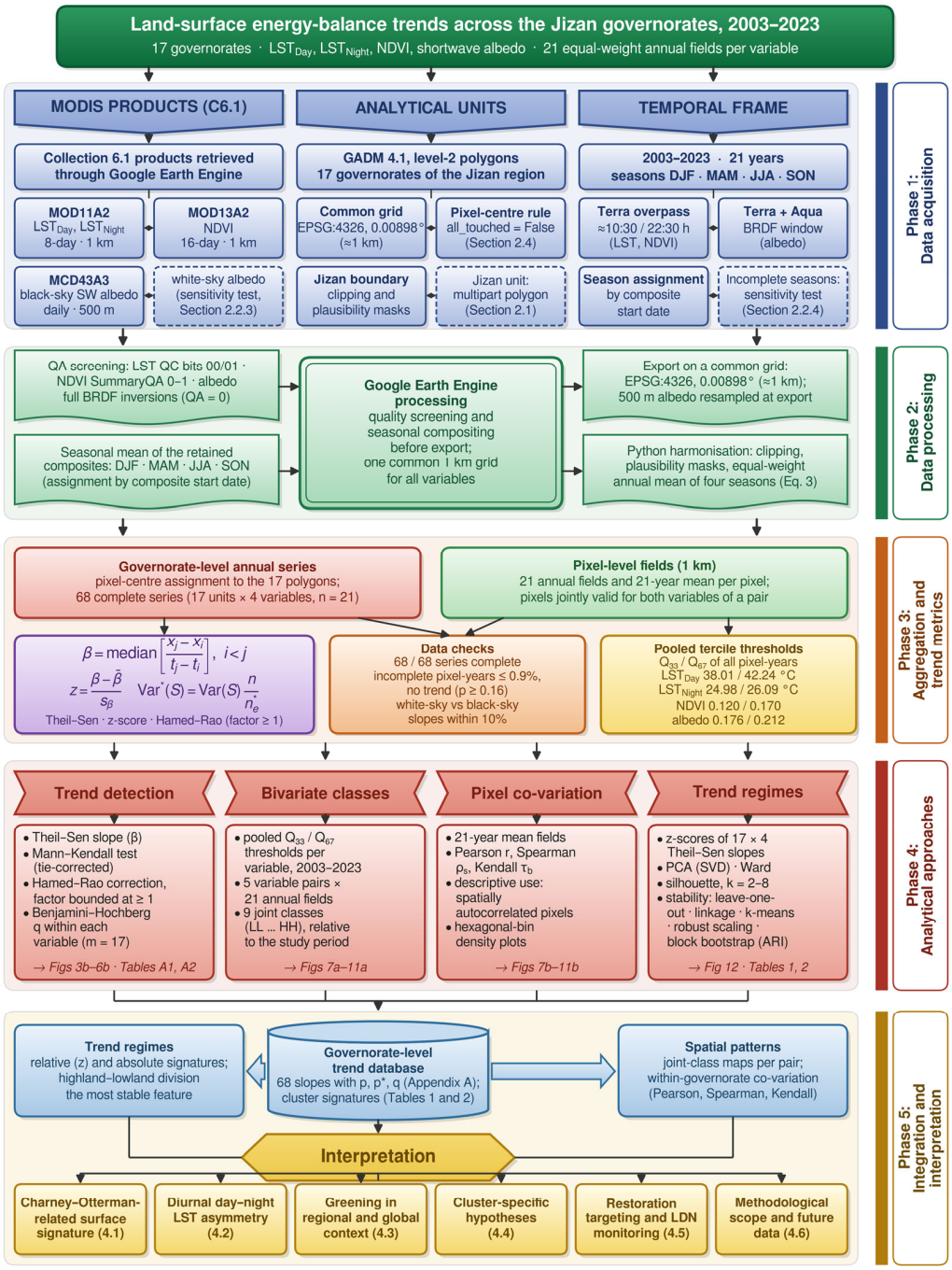


Figure 2. Methodological workflow of the study in five phases: (**1**) data acquisition, comprising the MODIS Collection 6.1 products, the administrative units and the temporal frame; (**2**) data processing, comprising quality screening, seasonal compositing and export in Google Earth Engine and spatial harmonisation and computation of the equal-weight annual fields in Python; (**3**) aggregation to governorate-level annual series and pixel-level fields, with the data checks, the trend and standardisation formulae and the pooled tercile thresholds; (**4**) analytical approaches, comprising trend detection, bivariate tercile classification, pixel-level co-variation and multivariate trend regimes with their stability tests; and (**5**) integration and interpretation. Colours distinguish the five phases. Solid boxes denote data, processing steps and analyses; dashed boxes denote sensitivity tests and dataset properties examined in the Methods. In the formula panel, β is the Theil–Sen slope, z the standardised slope (Equation (14)), Var*(S) the autocorrelation-corrected variance of the Mann–Kendall statistic and n^*_e the effective sample size (Section 2.5); p^* in the database symbol denotes the variance-corrected p-value. The input products are the MODIS Collection 6.1 datasets [20,24,61], the GADM 4.1 boundaries [59] and the Google Earth Engine platform [60]. The section numbers in the lowest row refer to the Discussion.

3. Results

3.1. Spatial Distribution and Trend Analysis of the Four Surface Variables

3.1.1. Daytime Land Surface Temperature

The 21 annual mean daytime LST maps (Figure 3a) reveal a spatially coherent altitudinal gradient that persists without structural disruption across the full study period. The Tihama coastal plain consistently registers values approaching 45 °C at the regional maximum, whereas the coolest parts of the Sarawat escarpment fall to about 28–30 °C, yielding a within-region thermal contrast of roughly 15 °C over a horizontal distance of less than 80 km. Intermediate values of 30–40 °C characterise the foothill transitional belt, and no detectable reorganisation of this three-zone thermal structure is observed in any of the 21 annual composites.

The per-governorate Theil–Sen estimates and Mann–Kendall tests (Figure 3b) show that daytime LST slopes are negative or close to zero in all 17 governorates. Statistically significant cooling ($p < 0.05$) occurs in five of them: Al Harth (-0.099 °C yr^{-1}, $p < 0.001$), Abu Arish (-0.060 °C yr^{-1}, $p = 0.012$), Al Aridah (-0.059 °C yr^{-1}, $p = 0.001$), Fayfa (-0.053 °C yr^{-1}, $p = 0.017$) and At Tuwal (-0.029 °C yr^{-1}, $p = 0.020$). After false-discovery-rate adjustment, the cooling remains significant in Al Harth and Al Aridah ($q = 0.007$ in both), whereas the three other governorates fall just above the adjusted threshold ($q = 0.068$). The variance-corrected test leaves all five results unchanged, because no significant positive autocorrelation was detected in the daytime series (Appendix A, Table A1). The remaining 12 governorates yield non-significant slopes between -0.046 °C yr^{-1} (Damad, $p = 0.057$) and $+0.000$ °C yr^{-1} (Jizan, $p = 1.000$). No governorate records a statistically significant daytime warming trend over the 21-year period.

3.1.2. Nighttime Land Surface Temperature

The annual mean nighttime LST maps (Figure 4a) reproduce the broad east-to-west altitudinal thermal structure observed for LST_{Day}, although the nocturnal range is considerably compressed, spanning roughly 16 °C to 30 °C across the regional colour scale, and the gradient between the Tihama plain and the Sarawat highlands is proportionally less steep than in the daytime field.

In contrast to the daytime signal, the per-governorate nighttime series (Figure 4b) document statistically significant warming in 16 of the 17 governorates ($p < 0.05$), all of which remain significant after false-discovery-rate adjustment ($q \leq 0.029$) and under the variance-corrected test. Theil–Sen slopes for the significant governorates range from $+0.030$ °C yr^{-1} (Al Aydabi, Al Harth) to $+0.077$ °C yr^{-1} (Abu Arish) and are systematically larger on the Tihama plain and along the coast ($+0.045$ to $+0.077$ °C yr^{-1} in Abu Arish, Ad Darb, Ahad Al Masarihah, At Tuwal, Baysh, Damad, Farasan, Jizan, Sabya and Samtah) than in the highland governorates ($+0.030$ to $+0.039$ °C yr^{-1} in Ad Dair, Al Aridah, Al Aydabi, Al Harth, Ar Rayth and Harub). Over the 2003–2023 period (20 years between the first and last observations), these slopes correspond to nighttime LST increases of about +0.6 to +1.5 °C. Fayfa ($+0.021$ °C yr^{-1}, $p = 0.057$) is the only governorate whose trend is not significant. No governorate records a statistically significant nighttime cooling trend.

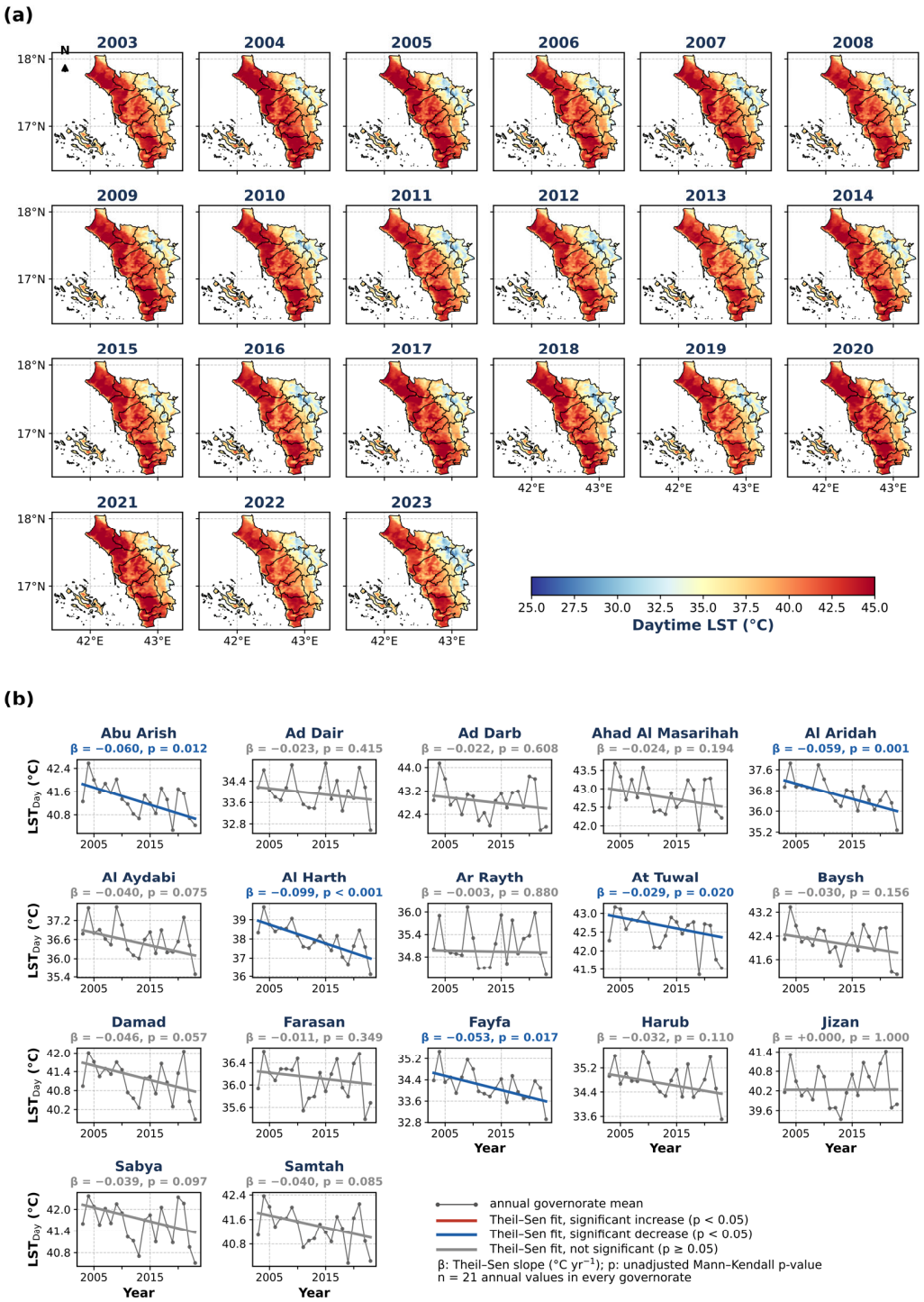


Figure 3. Daytime land surface temperature over the Jizan region, 2003–2023. (**a**) Annual mean MODIS Terra daytime LST (LST_{Day}, °C) for each year of the period; each panel represents the annual mean of one year, computed as the arithmetic average of the four seasonal composites (DJF, MAM, JJA, SON), clipped to the Jizan administrative boundary (black outline) and sharing the colour scale shown on the right. (**b**) Per-governorate annual mean daytime LST time series for the 17 governorates; each panel shows the annual values (filled circles connected by thin lines) and the Theil–Sen line, drawn in red for a significant increase, in blue for a significant decrease ($p < 0.05$) and in grey for a non-significant trend, as indicated in the legend panel. The line beneath each governorate name gives the Theil–Sen slope β (°C yr−1) and the unadjusted Mann–Kendall *p*-value; $n = 21$ annual values in every governorate. Adjusted and variance-corrected results are given in Appendix A.

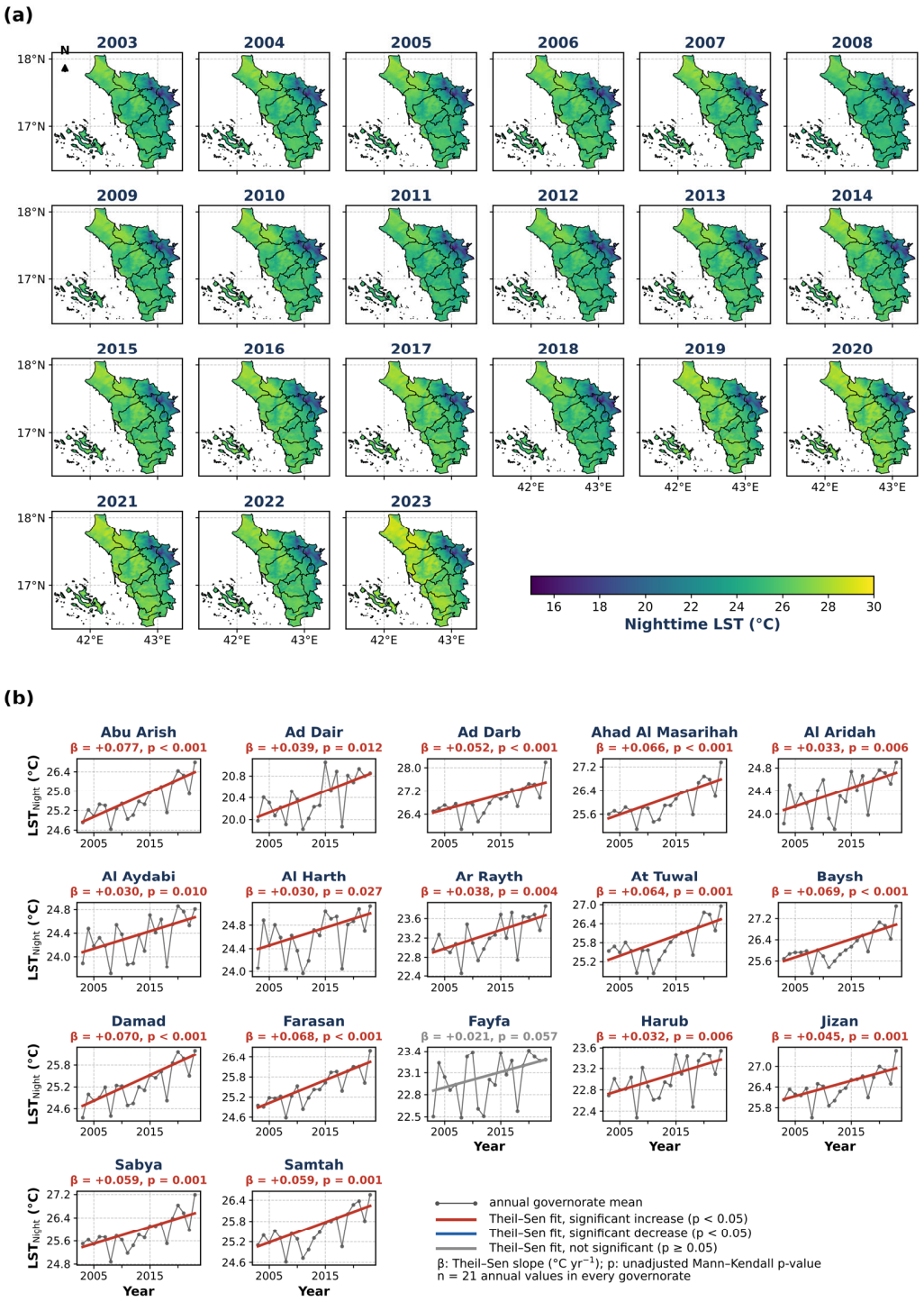


Figure 4. Nighttime land surface temperature over the Jizan region, 2003–2023. (**a**) Annual mean MODIS Terra nighttime LST (LST_{Night}, °C) for each year of the period. (**b**) Per-governorate annual mean nighttime LST time series for the 17 governorates, with Theil–Sen lines, line colours and statistical summaries as in Figure 3.

3.1.3. Vegetation Greenness According to the NDVI

The annual mean NDVI maps (Figure 5a) display a spatial distribution broadly complementary to LST_{Day}. Values below 0.10 characterise the Tihama coastal plain, the Sarawat escarpment records NDVI approaching 0.45 in its most densely vegetated areas, and the foothill belt occupies an intermediate range of about 0.10–0.25. This spatial organisation is consistent across all 21 annual composites.

The per-governorate trend analysis (Figure 5b) shows positive NDVI slopes in all 17 governorates ($p \leq 0.050$), all of which remain below the adjusted threshold ($q \leq 0.015$ in 16 governorates; in Farasan, whose slope is very small ($+0.0003\ yr^{-1}$), $p = q = 0.050$, at the margin of significance). The steepest slopes occur in the highland and escarpment governorates of Al Harth ($+0.0076\ yr^{-1}$), Fayfa ($+0.0067\ yr^{-1}$), Harub ($+0.0060\ yr^{-1}$) and Al Aridah ($+0.0058\ yr^{-1}$; $p \leq 0.001$ in all four), whereas the lowland governorates record slopes of about +0.0016 to $+0.0029\ yr^{-1}$, and the smallest slopes occur in Ad Darb ($+0.0010\ yr^{-1}$, $p = 0.014$) and Farasan. Under the variance-corrected test, Ahad Al Masarihah ($p = 0.012$) and Ar Rayth ($p = 0.005$) fall marginally short of significance ($p^* = 0.058$ and 0.052), and all other results are unchanged (Appendix A, Table A2). Over 2003–2023, the slopes correspond to NDVI increases of about +0.006 (Farasan) to +0.15 (Al Harth) NDVI units.

3.1.4. Shortwave Black-Sky Albedo

The annual mean shortwave black-sky albedo maps (Figure 6a) show the highest values, about 0.25–0.30, over the coastal sabkha and bare alluvial surfaces of the Tihama plain, and markedly lower values, mostly below 0.15, over the vegetated highland zone. This contrast is sustained throughout the 21-year record.

The per-governorate trend analysis (Figure 6b) reveals negative albedo slopes in all 17 governorates, statistically significant in 12 ($p \leq 0.050$). The steepest declines occur in Al Harth ($-0.0016\ yr^{-1}$, $p = 0.001$), Al Aridah ($-0.0011\ yr^{-1}$, $p = 0.002$), Abu Arish ($-0.0011\ yr^{-1}$, $p = 0.002$) and At Tuwal ($-0.0011\ yr^{-1}$, $p = 0.027$), and significant declines are also found in Ad Dair, Ahad Al Masarihah, Al Aydabi, Ar Rayth, Baysh, Harub, Sabya and Samtah. Damad, Fayfa, Ad Darb, Jizan and Farasan return non-significant slopes, that of Farasan being indistinguishable from zero ($p = 0.833$). After false-discovery-rate adjustment, seven declines remain significant (Abu Arish, Ad Dair, Al Aridah, Al Aydabi, Al Harth, Harub and Samtah; $q \leq 0.049$), while At Tuwal and Baysh lie marginally above the threshold ($q = 0.051$). The variance-corrected test is more restrictive for albedo, whose annual series show the strongest serial dependence: six governorates (Ahad Al Masarihah, Al Aridah, At Tuwal, Baysh, Harub and Sabya) lose significance, and the declines in Abu Arish, Ad Dair, Al Aydabi, Al Harth and Samtah remain significant under all three criteria (Appendix A, Table A2). Al Harth, which records the steepest decline, also records the strongest daytime cooling and the steepest NDVI increase.

3.2. Bivariate Tercile Classification and Pixel-Level Correlation

The 21-panel annual sequence of the LST_{Day} × NDVI bivariate tercile classification (Figure 7a) displays a spatially stable joint distribution throughout 2003–2023. The HL class (high LST_{Day}, low NDVI) dominates the Tihama coastal plain, and the LH class (low LST_{Day}, high NDVI) is consistently concentrated in the Sarawat highlands. The pooled tercile thresholds are $Q_{33}(LST_{Day}) \approx 38.01$ °C, $Q_{67}(LST_{Day}) \approx 42.24$ °C, $Q_{33}(NDVI) \approx 0.120$ and $Q_{67}(NDVI) \approx 0.170$.

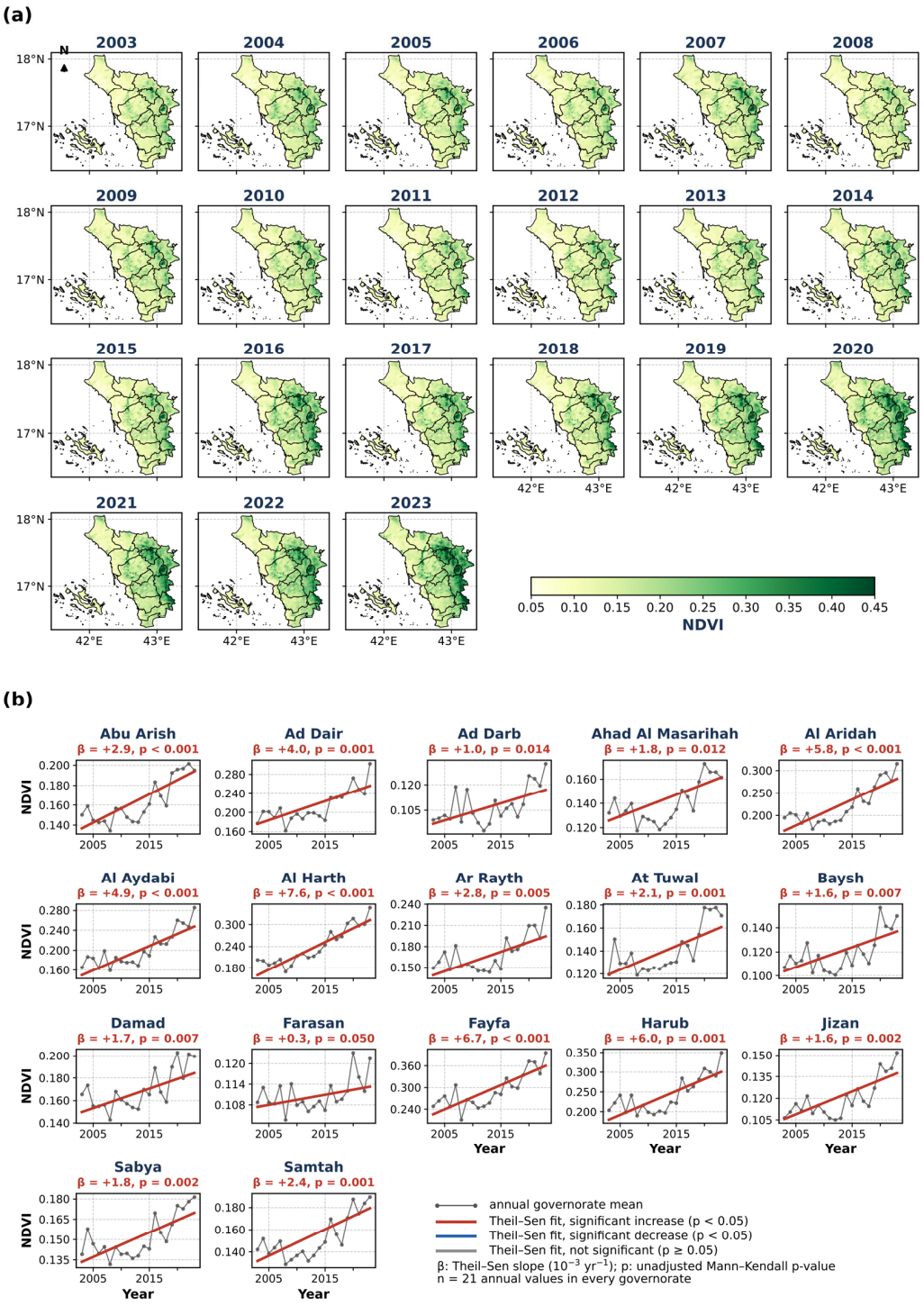


Figure 5. Vegetation greenness over the Jizan region, 2003–2023. (**a**) Annual mean NDVI (dimensionless) from the MOD13A2 product for each year of the period. (**b**) Per-governorate annual mean NDVI time series for the 17 governorates; line colours and the statistical summary beneath each governorate name are as in Figure 3, with the Theil–Sen slope β expressed in 10^{-3} NDVI units yr^{-1}.

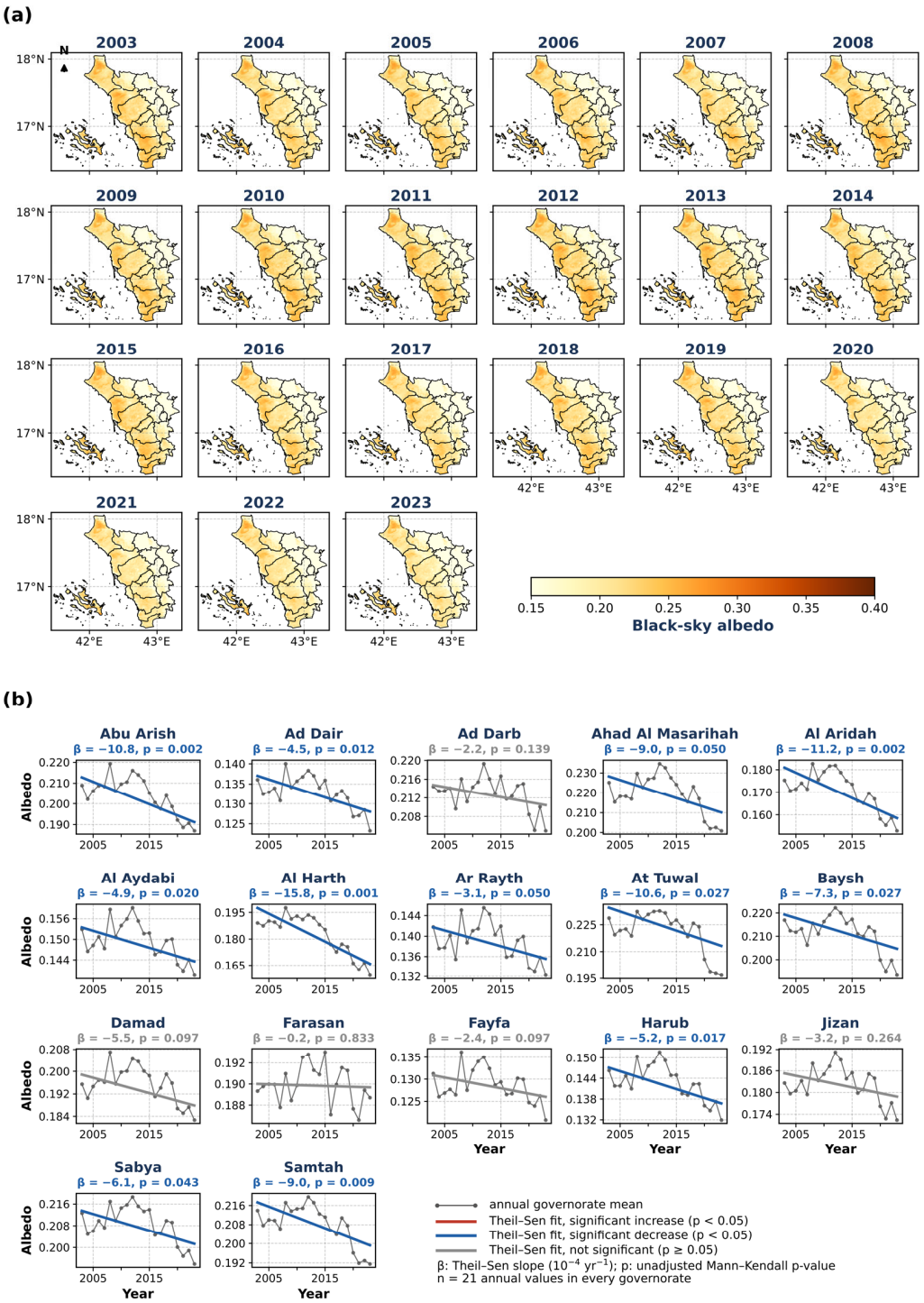


Figure 6. Shortwave broadband black-sky albedo over the Jizan region, 2003–2023. (**a**) Annual mean albedo (dimensionless) from the MCD43A3 product for each year of the period. (**b**) Per-governorate annual mean albedo time series for the 17 governorates; line colours and the statistical summary beneath each governorate name are as in Figure 3, with the Theil–Sen slope β expressed in 10^{-4} albedo units yr^{-1}.

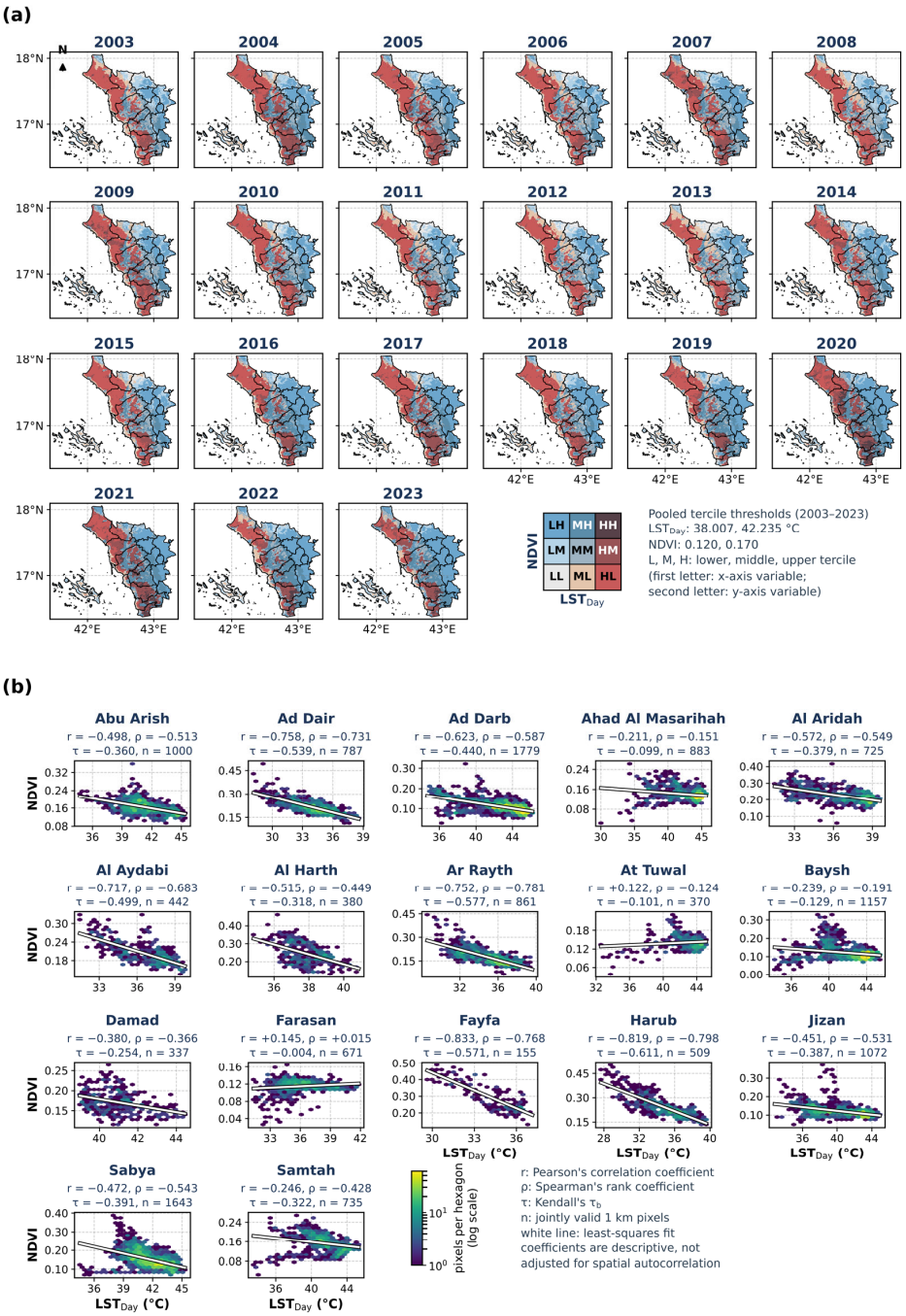


Figure 7. Joint distribution of daytime LST and NDVI across the Jizan region. (**a**) Annual bivariate tercile classification of LST_{Day} and NDVI for each year of the period 2003–2023; each pixel is assigned to one of nine joint classes (LL, LM, LH, ML, MM, MH, HL, HM, HH) on the basis of the pooled 33rd and 67th percentile thresholds, with the 3 × 3 bivariate legend and the pooled thresholds shown to the right of the panels. In each class label the first letter refers to the x-axis variable of the legend (LST_{Day}) and the second to the y-axis variable (NDVI), L, M and H denoting the lower, middle and upper tercile; each joint class has a fixed colour, grading from light grey (LL) through blue tones (increasing NDVI tercile) and red tones (increasing LST_{Day} tercile) to dark brown (HH), and white areas within the boundary are pixels without a valid value in that year. (**b**) Hexagonal-bin density scatter plots of pixel-level LST_{Day} against NDVI for each of the 17 governorates, computed on the 21-year mean fields; Pearson's r, Spearman's ρ_s and Kendall's τ_b (labelled τ) are annotated above each panel together with the pixel count n, the colour of each hexagon indicates the number of pixels it contains on a logarithmic scale (dark blue, one pixel; yellow, highest density; colour bar in the lower right), and the white line shows the least-squares linear fit; the coefficients are descriptive and are not adjusted for spatial autocorrelation (Section 2.7).

The pixel-level correlation analysis computed on the 21-year mean fields (Figure 7b) returns negative Pearson's r values in 15 of the 17 governorates. The strongest associations occur in the highland governorates of Fayfa ($r \approx -0.833$; $\rho_s \approx -0.768$; $\tau_b \approx -0.571$), Harub ($r \approx -0.819$; $\rho_s \approx -0.798$; $\tau_b \approx -0.611$), Ad Dair ($r \approx -0.758$; $\rho_s \approx -0.731$; $\tau_b \approx -0.539$), Ar Rayth ($r \approx -0.752$; $\rho_s \approx -0.781$; $\tau_b \approx -0.577$) and Al Aydabi ($r \approx -0.717$; $\rho_s \approx -0.683$; $\tau_b \approx -0.499$). Moderate negative correlations ($r \approx -0.45$ to -0.62) are found in Ad Darb, Al Aridah, Al Harth, Abu Arish, Sabya and Jizan, and weaker ones ($r \approx -0.21$ to -0.38) in Damad, Samtah, Baysh and Ahad Al Masarihah. At Tuwal ($r \approx +0.122$; $\rho_s \approx -0.124$; $\tau_b \approx -0.101$) and Farasan ($r \approx +0.145$; $\rho_s \approx +0.015$; $\tau_b \approx -0.004$) show essentially no association, and these are the only two governorates in which the three metrics do not agree in sign. Pixel counts range from $n = 155$ (Fayfa) to $n = 1779$ (Ad Darb).

The bivariate tercile maps for LST_{Day} × Albedo (Figure 8a) show the HH class (high LST_{Day}, high albedo) predominating on the Tihama coastal plain and the LL class (low LST_{Day}, low albedo) in the Sarawat highlands, a configuration sustained across all 21 panels. The pooled thresholds are $Q_{33}(LST_{Day}) \approx 38.01$ °C, $Q_{67}(LST_{Day}) \approx 42.24$ °C, $Q_{33}(\text{Albedo}) \approx 0.176$ and $Q_{67}(\text{Albedo}) \approx 0.212$.

The pixel-level scatter plots (Figure 8b) reveal positive Pearson's r values in 16 of the 17 governorates. The strongest correlations occur in Ahad Al Masarihah ($r \approx +0.894$), Samtah (+0.867), Harub (+0.865), Jizan (+0.845), Abu Arish (+0.838), At Tuwal (+0.825) and Al Aydabi (+0.814), that is, in most lowland governorates and in two highland ones. Weaker positive correlations occur in Ad Dair (+0.274), Ad Darb (+0.420) and Fayfa (+0.489), and Ar Rayth shows no association ($r \approx -0.033$; $\rho_s \approx +0.107$; $\tau_b \approx +0.100$); it is the only governorate in which the three metrics disagree in sign.

The LST_{Night} × NDVI bivariate maps (Figure 9a) reproduce the spatial structure observed for LST_{Day} × NDVI, with the LH class (low nighttime LST, high NDVI) in the highlands and the HL class (high nighttime LST, low NDVI) on the Tihama plain. The pooled nighttime LST thresholds are $Q_{33} \approx 24.98$ °C and $Q_{67} \approx 26.09$ °C; the NDVI thresholds are identical to those in Figure 7.

The hexagonal-bin scatter plots (Figure 9b) return negative pixel-level Pearson correlations between LST_{Night} and NDVI in all 17 governorates. The strongest occurs in Al Harth ($r \approx -0.890$; $\rho_s \approx -0.904$; $\tau_b \approx -0.729$), whose daytime association is only moderate ($r \approx -0.515$), followed by Harub ($r \approx -0.753$), Fayfa (−0.752), Sabya (−0.722), Damad (−0.714) and Ar Rayth (−0.696). Several lowland governorates show a markedly stronger nighttime than daytime coupling between surface temperature and vegetation (for example, Sabya, Damad and Ahad Al Masarihah). The weakest associations occur in Farasan ($r \approx -0.059$) and Ad Darb ($r \approx -0.163$); in Ad Darb, ρ_s and τ_b are weakly positive (+0.100 and +0.090), so that the three metrics agree in sign in 16 of the 17 governorates.

The LST_{Night} × Albedo bivariate maps (Figure 10a) display a more heterogeneous spatial distribution of joint classes than the LST_{Day} × Albedo pair (Figure 8a). The pooled thresholds are $Q_{33}(LST_{Night}) \approx 24.98$ °C, $Q_{67}(LST_{Night}) \approx 26.09$ °C, $Q_{33}(\text{Albedo}) \approx 0.176$ and $Q_{67}(\text{Albedo}) \approx 0.212$. The pixel-level scatter plots (Figure 10b) show predominantly positive but highly variable correlations. Pearson's r is positive in 15 governorates, ranging from strong values in Harub ($r \approx +0.811$), Al Aydabi (+0.638) and Jizan (+0.638) to negligible ones in Sabya (+0.057), Baysh (+0.100) and Ad Dair (+0.114), and it is weakly negative in Al Harth ($r \approx -0.049$) and Ar Rayth ($r \approx -0.155$); in Ar Rayth, ρ_s and τ_b are close to zero and positive. The coupling is much weaker than for the daytime pair (median $r \approx +0.26$, against +0.77 for LST_{Day} × Albedo), which is consistent with the weaker control exerted by shortwave reflectance on nocturnal surface temperature.

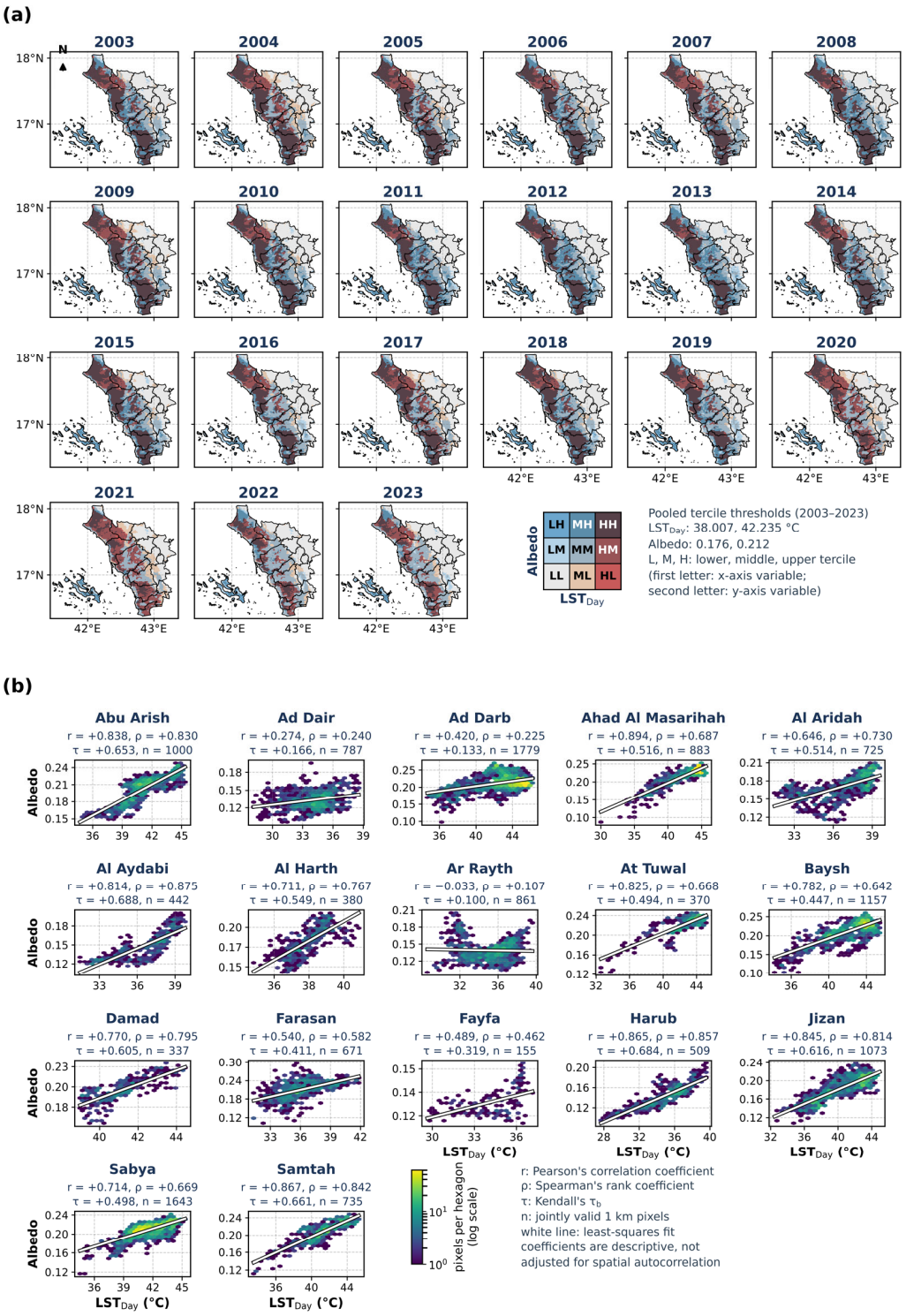


Figure 8. Joint distribution of daytime LST and shortwave black-sky albedo across the Jizan region. (**a**) Annual bivariate tercile classification of LST_{Day} and albedo for each year of the period 2003–2023. Class colours and legend conventions are as in Figure 7, with the first letter of each class referring to the x-axis variable and the second to the y-axis variable of the legend. (**b**) Hexagonal-bin density scatter plots of pixel-level LST_{Day} against albedo for each of the 17 governorates, computed on the 21-year mean fields. Statistical annotations, density scale and fitted line are as in Figure 7.

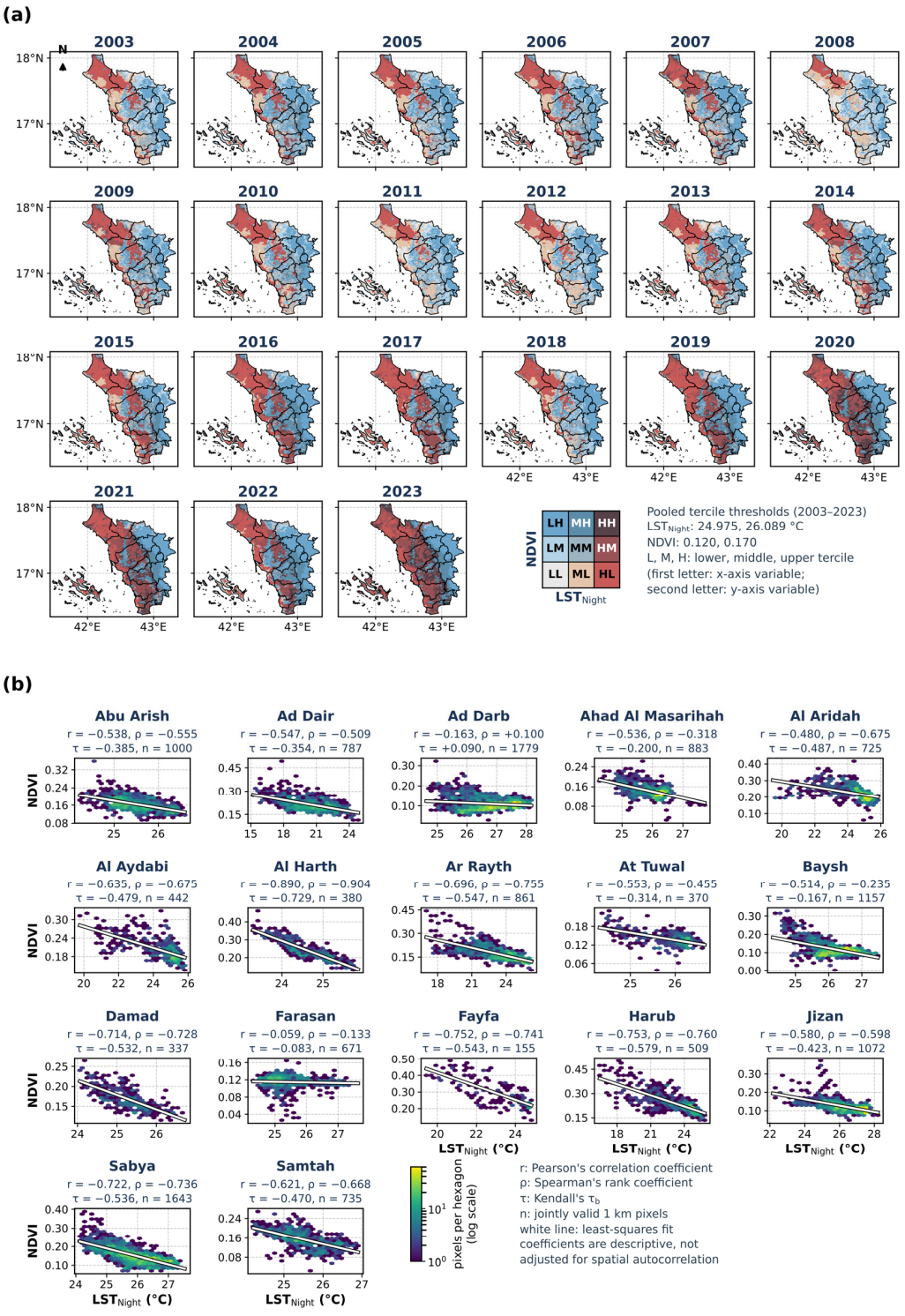


Figure 9. Joint distribution of nighttime LST and NDVI across the Jizan region. (**a**) Annual bivariate tercile classification of LST_{Night} and NDVI for each year of the period 2003–2023. Class colours and legend conventions are as in Figure 7, with the first letter of each class referring to the x-axis variable and the second to the y-axis variable of the legend. (**b**) Hexagonal-bin density scatter plots of pixel-level LST_{Night} against NDVI for each of the 17 governorates, computed on the 21-year mean fields. Statistical annotations, density scale and fitted line are as in Figure 7.

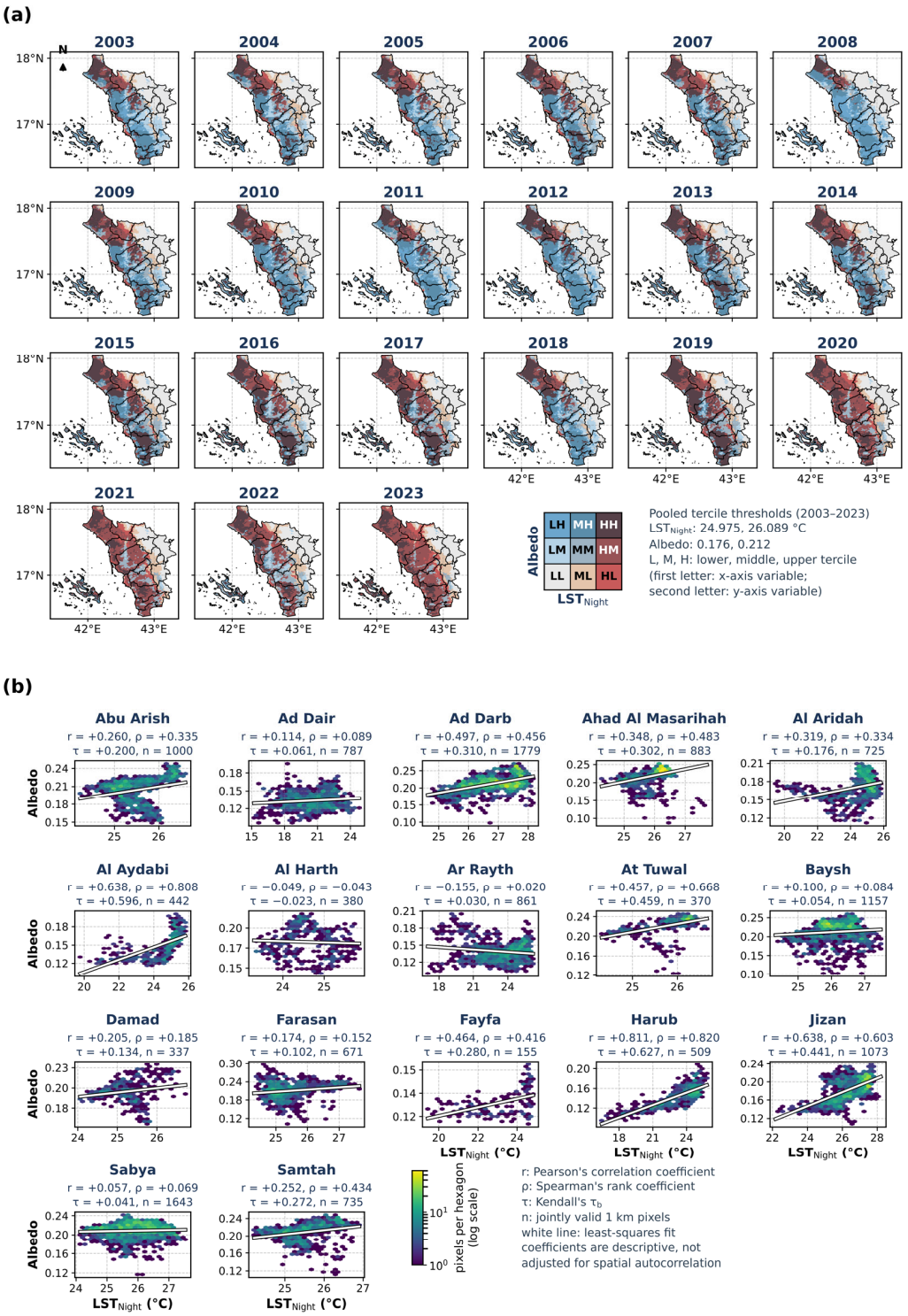


Figure 10. Joint distribution of nighttime LST and shortwave black-sky albedo across the Jizan region. (**a**) Annual bivariate tercile classification of LST_{Night} and albedo for each year of the period 2003–2023. Class colours and legend conventions are as in Figure 7, with the first letter of each class referring to the x-axis variable and the second to the y-axis variable of the legend. (**b**) Hexagonal-bin density scatter plots of pixel-level LST_{Night} against albedo for each of the 17 governorates, computed on the 21-year mean fields. Statistical annotations, density scale and fitted line are as in Figure 7.

The NDVI × Albedo bivariate maps (Figure 11a) exhibit a predominantly inverse spatial structure: the LH class (low NDVI, high albedo) characterises the Tihama plain and the HL class (high NDVI, low albedo) is concentrated in the Sarawat highlands. The pooled thresholds are Q_{33}(NDVI) ≈ 0.120, Q_{67}(NDVI) ≈ 0.170, Q_{33}(Albedo) ≈ 0.176 and Q_{67}(Albedo) ≈ 0.212. The pixel-level scatter plots (Figure 11b) return negative Pearson's r values in 15 governorates, with the strongest associations in Harub ($r \approx -0.673$), Al Aydabi (−0.550) and Abu Arish (−0.316) and values between −0.20 and −0.28 in nine others. Associations close to zero occur in At Tuwal ($r \approx +0.011$), Baysh (−0.061), Ar Rayth (−0.080) and Ad Darb (−0.084), and Farasan is the only governorate with a clear positive association ($r \approx +0.527$; $\rho_s \approx +0.194$; $\tau_b \approx +0.117$). The three metrics agree in sign in 14 of the 17 governorates, the exceptions being Ad Darb, Ar Rayth and At Tuwal.

3.3. Multivariate Trend Characterisation: PCA and Ward Hierarchical Clustering

PCA applied to the standardised 17 × 4 Theil–Sen slope matrix (Figure 12a) yields a compact two-dimensional solution in which PC1 accounts for 60.8% and PC2 for 32.8% of the total variance, the two components together explaining 93.6% of the multivariate trend variability. The loading vectors show that NDVI projects strongly onto the negative pole of PC1 while Albedo and LST_{Day} project onto the positive pole, establishing a principal axis of contrast between strong greening and weak or absent daytime cooling and albedo decline. Because the slopes were standardised, this axis is relative: governorates at its positive end are those in which daytime LST and albedo decreased least, not necessarily those in which they increased. LST_{Night} loads predominantly onto the negative pole of PC2 and thus constitutes an orthogonal dimension of trend variability that is largely independent of the NDVI–Albedo–LST_{Day} axis captured by PC1.

The Ward dendrogram (Figure 12b) and the silhouette analysis identify $k = 4$ as the optimal partition, the mean silhouette coefficient at this cut height exceeding those obtained for all other candidate values ($k = 2$, 3 and 5–8). The mean silhouette coefficient was 0.45 for $k = 4$, compared with 0.39 ($k = 2$), 0.40 ($k = 3$), 0.39 ($k = 5$) and 0.36 ($k = 6$), and it declined further for $k = 7$ and 8 (0.32 and 0.30). By the guideline of Kaufman and Rousseeuw [80], a value of 0.45 lies in the upper part of the 0.26–0.50 band and approaches the threshold of a reasonable structure (0.51); the partition is accordingly interpreted as a description of the dominant trend regimes rather than as a set of sharply separated classes. The mean silhouette widths of the individual clusters were 0.49 (Cluster 1), 0.21 (Cluster 2), 0.53 (Cluster 3) and 0.38 (Cluster 4). The spatial distribution of the four clusters is shown in Figure 12c, and the mean standardised Theil–Sen slopes and cluster compositions are reported in Table 1 and Figure 12d.

Cluster 1 ($n = 4$; Ad Dair, Al Aydabi, Fayfa, Harub) records mean standardised scores of $LST_{Day} = -0.05$, $LST_{Night} = -1.15$, NDVI = +1.03 and Albedo = +0.58. Three variables satisfy $|z| > 0.5$, namely LST_{Night} (−1.15), NDVI (+1.03) and Albedo (+0.58), indicating nighttime warming markedly weaker than the regional mean, greening stronger than the regional mean and an albedo decline weaker than the regional mean. In absolute terms (Table 2), all four members warmed at night (+0.021 to +0.039 °C yr^{-1}; significant in three), greened significantly (+0.0040 to +0.0067 yr^{-1}) and became darker (−0.0002 to −0.0005 yr^{-1}; significant in three); the positive albedo z-score therefore reflects a smaller decline, not an increase. The LST_{Day} score (−0.05) lies at the regional mean, which corresponds to an absolute cooling of −0.037 °C yr^{-1} on average (significant only in Fayfa).

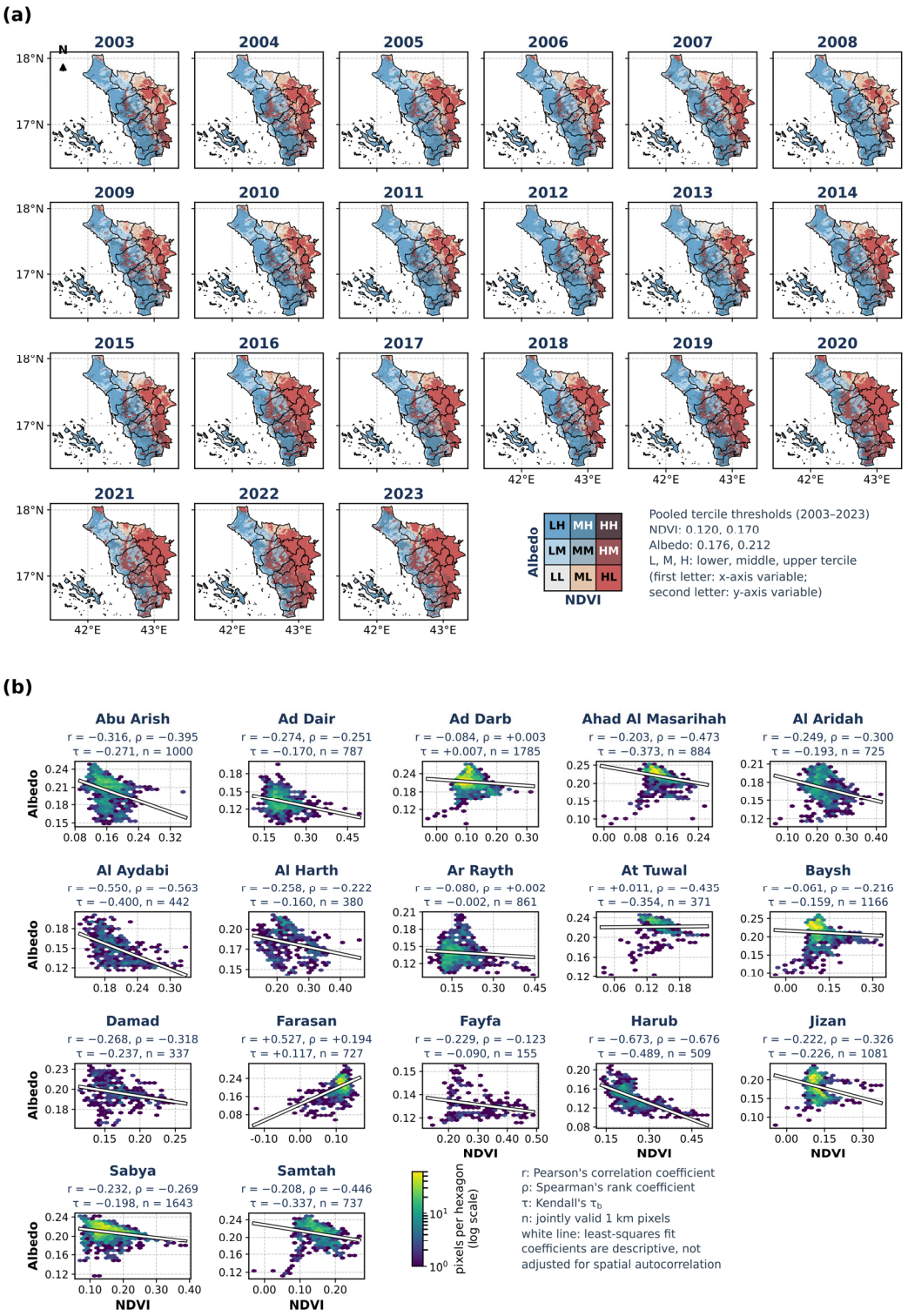


Figure 11. Joint distribution of NDVI and shortwave black-sky albedo across the Jizan region. (**a**) Annual bivariate tercile classification of NDVI and albedo for each year of the period 2003–2023. Class colours and legend conventions are as in Figure 7, with the first letter of each class referring to the x-axis variable and the second to the y-axis variable of the legend. (**b**) Hexagonal-bin density scatter plots of pixel-level NDVI against albedo for each of the 17 governorates, computed on the 21-year mean fields. Statistical annotations, density scale and fitted line are as in Figure 7.

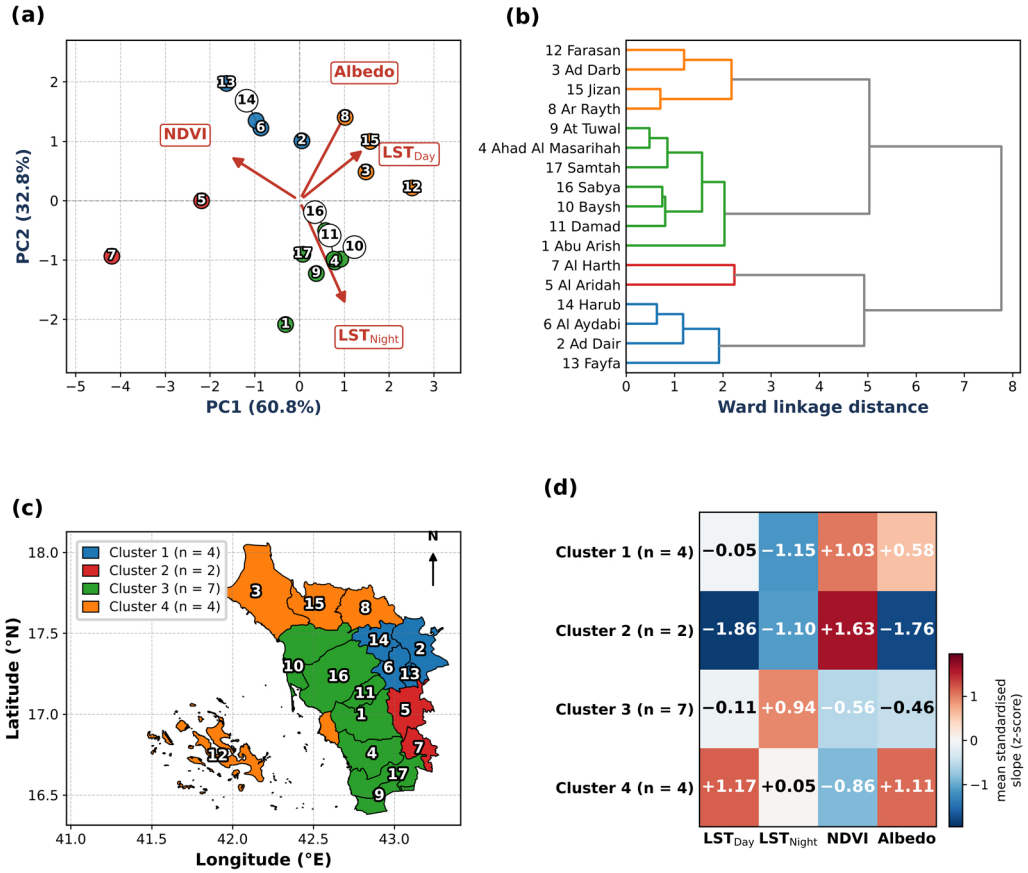


Figure 12. Multivariate trend characterisation of the 17 Jizan governorates, 2003–2023. (**a**) PCA biplot showing the projection of the governorates onto the first two principal components computed from the standardised Theil–Sen slopes of LST_{Day}, LST_{Night}, NDVI and Albedo; each governorate is plotted as a numbered marker coloured by cluster assignment, the red arrows indicate the loading direction and magnitude of each variable, and the explained variance ratio of each component is given in the axis labels. (**b**) Ward hierarchical dendrogram constructed on the standardised feature matrix using Euclidean distance and the minimum-variance linkage criterion; branch colours correspond to the terminal cluster assignment at the silhouette-optimal cut height and match the colours used in panels (**a**,**c**,**d**). (**c**) Choropleth map of the governorates coloured by cluster assignment, with numbered labels; the numbers identify the governorates as listed in panel (**b**). (**d**) Cluster trend-signature heatmap displaying the mean standardised Theil–Sen slope of each variable within each cluster with explicit numeric annotation; red shading indicates positive and blue shading negative standardised trends (relative to the regional mean; absolute slopes are given in Table 2).

Cluster 2 ($n = 2$; Al Aridah, Al Harth) returns the most extreme standardised magnitudes of any cluster, with $LST_{Day} = -1.86$, $LST_{Night} = -1.10$, NDVI = +1.63 and Albedo = −1.76. All four variables satisfy $|z| > 0.5$, signifying the most negative daytime LST tendency, a nighttime LST tendency close to that of Cluster 1, the strongest greening signal among the 17 governorates and the most strongly negative albedo trend in the dataset. In absolute terms, both members cooled significantly by day (−0.059 and −0.099 °C yr^{-1}) but warmed significantly at night (+0.033 and +0.030 °C yr^{-1}); the negative LST_{Night} z-score therefore denotes weaker-than-average nocturnal warming, not nocturnal cooling.

Cluster 3 ($n = 7$; Abu Arish, Ahad Al Masarihah, At Tuwal, Baysh, Damad, Sabya, Samtah), the largest cluster and composed mainly of governorates on the Tihama lowland and the lower foothill belt, returns mean scores of $LST_{Day} = -0.11$, $LST_{Night} = +0.94$, NDVI = −0.56 and Albedo = −0.46. The variables with $|z| > 0.5$ are LST_{Night} (+0.94) and NDVI (−0.56), reflecting above-average nighttime warming paired with a below-average greening trend, while LST_{Day} and Albedo remain closer to the regional mean. In absolute

terms, all seven members warmed significantly at night (+0.059 to +0.077 °C yr^{-1}) and greened significantly (+0.0016 to +0.0029 yr^{-1}), so the negative NDVI z-score denotes slower greening, not browning. Albedo declined in all seven (significantly in six), and daytime LST declined in all seven (significantly in Abu Arish and At Tuwal).

Cluster 4 (n = 4; Ad Darb, Ar Rayth, Farasan, Jizan) records standardised scores of LST_{Day} = +1.17, LST_{Night} = +0.05, NDVI = −0.86 and Albedo = +1.11, with LST_{Day}, NDVI and Albedo satisfying $|z| > 0.5$. This cluster carries the highest relative daytime LST tendency, the weakest greening and the weakest albedo decline of any cluster. These are relative positions. In absolute terms (Table 2), no member warmed significantly by day (slopes −0.022 to +0.000 °C yr^{-1}), all four greened (+0.0003 to +0.0028 yr^{-1}; significant in all four, marginally so in Farasan), and albedo decreased slightly or remained stable (−0.0003 to 0.0000 yr^{-1}; significant only in Ar Rayth, $p = 0.050$). Cluster 4 therefore shows no absolute warming, browning or brightening; it is distinguished by the absence of the daytime cooling and darkening that accompany greening in the other clusters. Its LST_{Night} score (+0.05) lies at the regional mean, in contrast to the strongly negative or strongly positive LST_{Night} signals of Clusters 1, 2 and 3. Geographically, the cluster combines three northern governorates (Ad Darb on the coast, Jizan and the mountainous Ar Rayth) with the Farasan archipelago (Figure 12c).

Table 2 reports the same cluster means in physical units together with the number of members whose trend is significant. Read together with Table 1, it shows that the relative signatures and the absolute changes differ in several cases: the negative LST_{Night} z-scores of Clusters 1 and 2 correspond to significant nocturnal warming, the negative NDVI z-scores of Clusters 3 and 4 to significant greening, and the positive albedo z-scores of Clusters 1 and 4 to weak declines. Only the daytime LST signal of Cluster 4, which is essentially flat, departs from the regional pattern of daytime cooling.

Table 1. Cluster composition and trend signatures of the 17 Jizan governorates from Ward hierarchical clustering of the four-variable standardised Theil–Sen slope matrix. Columns report the cluster identifier, the number of member governorates, the member governorates, the mean standardised slope (z-score) of LST_{Day}, LST_{Night}, NDVI and Albedo within each cluster, and a verbal relative trend signature listing the variables with $|z| > 0.5$; absolute slopes are given in Table 2.

Cluster	n	Member Governorates	LST_{Day} (z)	LST_{Night} (z)	NDVI (z)	Albedo (z)	Relative Trend Signature
1	4	Ad Dair, Al Aydabi, Fayfa, Harub	−0.05	**−1.15**	**+1.03**	**+0.58**	LST_{Night} ↓, NDVI ↑, Albedo ↑
2	2	Al Aridah, Al Harth	**−1.86**	**−1.10**	**+1.63**	**−1.76**	LST_{Day} ↓, LST_{Night} ↓, NDVI ↑, Albedo ↓
3	7	Abu Arish, Ahad Al Masarihah, At Tuwal, Baysh, Damad, Sabya, Samtah	−0.11	**+0.94**	**−0.56**	−0.46	LST_{Night} ↑, NDVI ↓
4	4	Ad Darb, Ar Rayth, Farasan, Jizan	**+1.17**	+0.05	**−0.86**	**+1.11**	LST_{Day} ↑, NDVI ↓, Albedo ↑

Silhouette-optimal cluster count k = 4. Standardised slopes are the z-scores of each governorate's Theil–Sen slope relative to the 17-governorate distribution; values with $|z| > 0.5$ are shown in bold. Positive scores indicate above-average and negative scores below-average trend magnitudes. Arrows in the trend signature refer to the relative (standardised) tendency, not to the absolute sign of the slope. Cluster colours match Figure 12. The threshold $|z| > 0.5$ corresponds to half a between-governorate standard deviation (Section 2.8); variables with $|z|$ between 0.4 and 0.6 (Albedo in Cluster 1; NDVI and Albedo in Cluster 3) are secondary features of the signatures.

Table 2. Mean absolute Theil–Sen slopes of the four variables in each cluster, with the range across member governorates in parentheses and the number of members with a significant trend (unadjusted Mann–Kendall $p \leq 0.05$) after the semicolon.

Cluster	LST_{Day} (°C yr^{-1})	LST_{Night} (°C yr^{-1})	NDVI (10^{-3} yr^{-1})	Albedo (10^{-4} yr^{-1})
1 (Ad Dair, Al Aydabi, Fayfa, Harub)	−0.037 (−0.053 to −0.023); 1/4	+0.031 (+0.021 to +0.039); 3/4	+5.4 (+4.0 to +6.7); 4/4	−4.3 (−5.2 to −2.4); 3/4
2 (Al Aridah, Al Harth)	−0.079 (−0.099 to −0.059); 2/2	+0.031 (+0.030 to +0.033); 2/2	+6.7 (+5.8 to +7.6); 2/2	−13.5 (−15.8 to −11.2); 2/2
3 (Abu Arish, Ahad Al Masarihah, At Tuwal, Baysh, Damad, Sabya, Samtah)	−0.038 (−0.060 to −0.024); 2/7	+0.066 (+0.059 to +0.077); 7/7	+2.0 (+1.6 to +2.9); 7/7	−8.3 (−10.8 to −5.5); 6/7
4 (Ad Darb, Ar Rayth, Farasan, Jizan)	−0.009 (−0.022 to 0.000); 0/4	+0.051 (+0.038 to +0.068); 4/4	+1.4 (+0.3 to +2.8); 4/4	−2.2 (−3.2 to −0.2); 1/4
All 17 governorates	−0.036 (−0.099 to 0.000)	+0.050 (+0.021 to +0.077)	+3.2 (+0.3 to +7.6)	−6.5 (−15.8 to −0.2)

LST values are averages of the slopes reported in Figures 3b and 4b. NDVI and albedo values were computed from the slopes underlying Figures 5b and 6b at full precision. The last row gives the regional mean against which the *z*-scores of Table 1 are computed.

The four-cluster partition was largely insensitive to the analytical choices examined. Omitting any one governorate left the partition of the remaining 16 unchanged in 16 of 17 cases (the exception being the omission of the Jizan unit, after which Ad Dair moved to Cluster 4; ARI = 0.87). Complete linkage and *k*-means reproduced the partition exactly (ARI = 1.00), and average linkage and robust standardisation reproduced it except that Al Aridah joined Cluster 1 and Al Harth formed a cluster of its own (ARI = 0.90). When the uncertainty of the trend estimates was propagated by the block bootstrap, the median ARI between the bootstrap and original partitions was 0.55 (interquartile range 0.39–0.72), and the mean co-assignment frequency of cluster members was 0.71, 0.54, 0.69 and 0.77 for Clusters 1–4, respectively. The two-cluster solution, which separates the eastern highland and escarpment governorates (Clusters 1 and 2) from the lowland, northern and insular governorates (Clusters 3 and 4), was selected in about half of the replicates and the four-cluster solution in 17%. The highland–lowland division is therefore the most robust feature of the trend space, and the four regimes refine it into groups that differ in the strength of their recovery signal; the finer distinctions between regimes are interpreted accordingly in Section 4.4. Across $|z|$ thresholds of 0.4–0.75, the core signatures were unchanged (Cluster 1: LST_{Night} and NDVI; Cluster 2: all four variables; Cluster 3: LST_{Night}; Cluster 4: LST_{Day}, NDVI and Albedo), and only the secondary features listed in the note to Table 1 entered or left the signatures; at $|z| > 1.0$, the Cluster 3 signature became empty and NDVI left the Cluster 4 signature.

4. Discussion

4.1. Departure from the Charney–Otterman-Related Surface Signature

The Charney–Otterman framework postulates that vegetation removal in arid regions elevates surface albedo, which drives radiative cooling of the atmospheric column, induces subsidence and suppresses convective precipitation, thereby favouring further vegetation loss [5,6]. Its land-surface expression comprises falling vegetation cover and rising reflectance, whereas the accompanying change in daytime surface temperature is ambiguous: brightening alone reduces absorbed radiation and cools the surface, the loss of evapotranspiration warms it [7], and comparisons across grazing boundaries have recorded both cooler [5] and warmer [89] degraded surfaces. Satellite-based degradation diagnostics usually adopt the combination of rising daytime LST, falling NDVI and rising albedo as the degradation signature. It is this Charney–Otterman-related surface signature, rather

than the complete feedback, that the present analysis evaluates; the atmospheric limbs of the loop (column cooling, subsidence and rainfall suppression) lie outside the scope of a land-surface diagnostic. Across the Jizan region the diagnostic signatures returned by the four MODIS variables point in the opposite direction: a universal positive NDVI trend, a widespread reduction in shortwave albedo and a daytime LST signal that is either statistically stable or significantly negative. This configuration is the reverse of the degradation signature and resembles the patterns reported for other dryland systems in which land-surface modification has proceeded through irrigation expansion, urban greening or natural vegetation recovery rather than through cover removal [3,10,11,58]. From the perspective of dryland resilience, the Jizan record therefore documents a system in which recovery-consistent trajectories of differing strength, rather than opposing degradation and recovery trajectories, coexist within a single administrative region.

The persistence of the inverted pattern across all seventeen governorates in absolute terms indicates that the Tihama–Sarawat system as a whole is not undergoing Charney-style desertification over the 2003–2023 window. The two governorates of Cluster 2 (Al Aridah and Al Harth) carry the strongest expression of this inversion, with the most negative standardised daytime LST tendency, the most pronounced greening of any cluster and the largest decrease in albedo. Cluster 4 (Ad Darb, Ar Rayth, Farasan and Jizan) occupies the opposite end of the trend space and is the only cluster whose relative tendencies point towards the degradation signature. Its absolute trends, however, show no daytime warming, a weak but significant greening and a near-stable albedo (Table 2), and none of its members exhibits warming, browning and brightening together. Cluster 4 is therefore better described as a regime of lagging recovery, in which greening has been too weak to be accompanied by the daytime cooling and darkening observed elsewhere, than as an actively degrading system. No governorate in the region shows the absolute Charney–Otterman-related surface signature. This stratification implies that a region-averaged diagnostic would mask substantial differences in the strength of the recovery signal, and it underlines the value of governorate-scale clustering over conventional area-averaged trend analysis [7,13] for any assessment intended to inform land management.

4.2. Diurnal Asymmetry as a Diagnostic of Surface-Property Change

A central finding is the systematic divergence between daytime and nighttime LST trends. Statistically significant warming was returned in 16 of 17 governorates for LST_{Night} but in none for LST_{Day}, while five governorates registered significant daytime cooling (two after false-discovery-rate adjustment). This pattern replicates at the regional scale the global signature of disproportionate nocturnal warming documented over recent decades [37–39]. Whereas the planetary-scale asymmetry has been attributed mainly to greenhouse-gas-driven longwave forcing in combination with changes in cloud cover and atmospheric water vapour [36], the magnitude of the night–day contrast in Jizan, which is at least 0.09 °C yr^{-1} in all seven governorates of Cluster 3 and reaches 0.137 °C yr^{-1} in Abu Arish and 0.129 °C yr^{-1} in Al Harth, is consistent with a surface-property contribution superimposed on the background radiative trend, the relative size of which could be quantified with collocated soil-moisture and radiation data.

Several coupled mechanisms are consistent with this asymmetry, although none of them is identified by the satellite variables themselves. The simultaneous greening and albedo reduction are consistent with higher vegetation cover and lower bare-soil exposure, which would be expected to enhance daytime evapotranspirative cooling while raising soil thermal inertia and nocturnal heat release [29,30]. Where irrigated agriculture has expanded in the Tihama corridor [52], higher near-surface humidity and soil moisture would likewise be expected to compress the diurnal temperature range through thermal-inertia and latent-

heat-flux pathways [40]; irrigated extent and soil moisture are not, however, among the variables analysed here. Urban expansion in Jizan City and adjacent administrative centres may add a nocturnally biassed heat-island signal [13,53,90,91]. Nocturnal warming is, however, weaker in Cluster 4, which contains the Jizan unit, than in the predominantly rural lowland governorates of Cluster 3 (Table 2); the 1 km governorate means cannot isolate urban pixels, and the Jizan unit itself consists mainly of inland terrain north of Baysh (Section 2.1). Urban heat-island effects are therefore unlikely to account for the regional signal, and moisture- and vegetation-mediated mechanisms are the more plausible candidates, a hypothesis that requires soil-moisture, irrigation and land-cover data to test. The asymmetric thermal response thus emerges as a more discriminating indicator of change in surface properties than either LST variable considered alone, and it supports the retention of day and night fields as complementary diagnostics in dryland surface-energy-balance studies [30,41,42,92].

4.3. Regional Greening in Continental and Global Context

The detection of positive NDVI trends in all 17 governorates, significant after adjustment for multiple testing (marginally so in Farasan), situates Jizan within the broader regional and global greening pattern, in which substantial fractions of vegetated land, and semi-arid and arid environments in particular, have shown net increases in leaf area and NDVI over recent decades [10,11]. The cumulative NDVI increases derived from the Theil–Sen slopes, of about +0.006 to +0.15 NDVI units over 2003–2023, are comparable in magnitude to those reported for the Sahel and the Horn of Africa over the longer 1981–2007 window [9] and align both with the agricultural greening documented for irrigated districts elsewhere in Saudi Arabia [52] and with the reduction in desertification severity mapped across the Jizan province between 2001 and 2020 [58].

Several non-mutually exclusive drivers can be invoked, none of which can be confirmed or excluded from the satellite variables alone. The carbon dioxide fertilisation hypothesis [8] predicts that warm, arid environments respond disproportionately to rising atmospheric CO_2 through reductions in stomatal conductance and gains in plant water-use efficiency, which provides a baseline mechanism for diffuse greening across non-managed surfaces. Superimposed on this background, the expansion and intensification of agriculture is a plausible local driver. The steepest positive NDVI slopes (Al Harth, Fayfa, Harub and Al Aridah) occur in highland and escarpment governorates where terraced agriculture is long established, whereas the slopes in the irrigated lowland governorates are smaller; this pattern suggests that the highland terrace systems and the higher rainfall of the escarpment may contribute more to the greening than lowland irrigation, a hypothesis that can be tested with rainfall and land-use records. Recent Saudi afforestation and urban greening initiatives, including those launched under the Vision 2030 framework, may add to the later part of the trajectory, although the 21-year window largely pre-dates the most intensive afforestation phases [58]. The weakest greening occurs in the Cluster 4 governorates of Farasan and Ad Darb. Impervious-surface expansion, coastal salinisation or limited water availability could attenuate vegetation gains there, but these explanations remain to be tested with land-cover and water-use data.

Disentangling the relative contributions of CO_2 fertilisation, irrigated-agriculture expansion, urban afforestation and interannual precipitation variability would require coupling the NDVI trajectories to spatially explicit irrigation, land-cover-change and rainfall datasets. Such coupling is a natural extension of the present satellite-based framework and is particularly valuable given the sparse in situ meteorological network in the southwestern Saudi Arabian highlands and the resulting reliance on satellite diagnostics for both monitoring and attribution [43,45].

4.4. Cluster-Specific Interpretation

Three of the four trend regimes recovered by the PCA–Ward analysis correspond to coherent physiographic units (the northeastern highlands, the southeastern escarpment and the Tihama lowlands), whereas the fourth groups three northern governorates with the Farasan archipelago. This correspondence is consistent with the view that surface-energy-balance evolution in Jizan is shaped by topographic, hydrological and anthropogenic gradients rather than by a single dominant forcing. Because the highland–lowland division is the most robust feature of the partition (Section 3.3), the interpretations offered below for individual clusters are framed as hypotheses for further testing.

Cluster 2 (Al Aridah, Al Harth), located along the western escarpment of the Sarawat highlands, displays the most pronounced inversion of the Charney–Otterman-related surface signature. Orographically enhanced precipitation along the escarpment [45,55], terraced agricultural systems with a long history of intensive land management, and cooler conditions at altitude may jointly favour vegetation expansion, evapotranspirative daytime cooling and progressive replacement of bare-soil reflectance by darker canopy reflectance. The small membership of the cluster ($n = 2$) is consistent with the limited spatial extent of the escarpment zone in which these conditions converge; its low mean silhouette width (0.21) also indicates that the two members are less tightly grouped than those of the other clusters. If confirmed with land-use data, its behaviour would illustrate how traditional terrace-based land management can sustain a recovery-consistent trajectory under contemporary climatic stress.

Cluster 1 (Ad Dair, Al Aydabi, Fayfa, Harub) represents a milder expression of the same highland regime, with above-average greening and a strongly below-average nighttime warming tendency but a near-mean daytime LST signal. Its positive albedo z-score corresponds to an absolute decline that is smaller than the regional mean (Table 2), not to brightening. A plausible explanation is that these highland surfaces were already dark at the start of the record (governorate mean black-sky albedo of 0.13–0.15, against 0.19–0.22 in the lowland governorates; Figure 6b), leaving less scope for further darkening as vegetation increased; this interpretation warrants verification through high-resolution land-cover analysis.

Cluster 3 (Abu Arish, Ahad Al Masarihah, At Tuwal, Baysh, Damad, Sabya, Samtah) encompasses the densely irrigated portion of the Tihama plain and the lower foothill belt. The combination of pronounced nighttime warming with a below-average vegetation trend, although the NDVI slope remains positive in absolute terms, is consistent with a system in which diurnal-range compression dominates over the magnitude of greening, possibly reflecting a heat-storage feedback from soil-moisture redistribution under intensified groundwater-based irrigation [40]. This interpretation requires irrigation and soil-moisture data to test. The presence of several of the most populous administrative units in this cluster, and the possibility that its greening depends on groundwater, a resource that is itself under pressure [50], give it particular relevance for water governance and for the long-term sustainability of the greening it exhibits.

Cluster 4 (Ad Darb, Ar Rayth, Farasan, Jizan) is the regime whose relative tendencies lie closest to the Charney–Otterman-related surface signature, but its absolute trends indicate lagging recovery rather than degradation (Section 4.1). The cluster is geographically heterogeneous: it combines the northern coastal governorate of Ad Darb, the Jizan unit, the mountainous Ar Rayth and the Farasan archipelago, so that no single land-use process is likely to explain its signature. Coastal salinisation and limited freshwater availability on Farasan and along the coast [57] and impervious-surface expansion around urban centres [13,53] are candidate explanations for the weak greening and the absence of daytime cooling in parts of the cluster. Because the Jizan unit of the boundary dataset is dominated

by an inland block north of Baysh (Section 2.1) and contains only a small coastal part around Jizan City, its governorate mean cannot be read as an urban signal. Although this cluster comprises only 24% of the analysed administrative units, it is where the recovery signal is weakest, and it is therefore a logical first target for land-cover and water-use investigations designed to establish whether the lag reflects a temporary delay or an emerging divergence.

4.5. Implications for Dryland Resilience, Restoration Targeting and Nature-Based Solutions

The results carry implications for how resilience is assessed and how restoration is targeted in dryland administrative units. Because the strength of the recovery signal varies markedly between governorates, region-wide interventions calibrated to an average condition would misallocate effort, treating strongly recovering governorates in the same way as those in which recovery is lagging. Read together with the stability analysis of Section 3.3, the governorate-scale clustering provides a starting point for differentiated management, in which the Cluster 4 governorates become priorities for diagnosing why greening is weak and, where appropriate, for coastal vegetation restoration, while Clusters 1 and 2 become candidates for protecting and extending the terrace-based land management that may underpin their recovery.

The findings also qualify the interpretation of greening as an unambiguous sign of resilience. In Cluster 3 the greening is coupled to pronounced nighttime warming; whether it also depends on groundwater-fed irrigation cannot be determined from the satellite variables alone. A recovery signal that depended on the depletion of a non-renewable water resource [50] would not be resilient in the sense intended by land-degradation-neutrality frameworks [2], and the diurnal-asymmetry diagnostic introduced here, once combined with independent soil-moisture and irrigation data, could offer a means of distinguishing moisture-subsidised greening from greening sustained by rainfall and land management. Nature-based solutions such as rain-fed afforestation, terrace rehabilitation, wadi-bank vegetation buffers and coastal mangrove or halophyte restoration are more consistent with the escarpment regime than with the irrigated lowland regime, and the satellite diagnostic can be re-run at low cost to evaluate whether such measures shift a governorate from a lagging to a stronger recovery-consistent signature. In this respect the framework serves both as a baseline against which the Saudi Green Initiative and related programmes can be assessed and as a monitoring instrument for their subsequent evaluation.

4.6. Methodological Considerations and Future Directions

The thermal analysis is based on the Terra overpasses (about 10:30 and 22:30 local solar time), which coincide with the overpass of the MOD13A2 vegetation product and thus keep the thermal and vegetation records on the same platform. Adding the Aqua overpasses (about 13:30 and 01:30 local solar time) from the MYD11A2 product would sample the diurnal cycle closer to the times of maximum and minimum surface temperature and would provide an independent check on the day–night asymmetry reported here [17]. Because ground stations are sparse in the Jizan region, a persistent gap in the climatology of southwestern Saudi Arabia [43], satellite diagnostics of the kind developed here are currently the principal source of spatially continuous evidence on surface-energy-balance change in the region.

The framework is diagnostic rather than attributional. It establishes the direction, magnitude and spatial organisation of the trends, and the mechanisms invoked in Sections 4.2–4.4 are hypotheses consistent with these patterns rather than demonstrated causes. Testing them, and partitioning the greening among agricultural intensification, urban expansion, CO_2 fertilisation and rainfall variability, requires the four MODIS variables to be coupled with gridded precipitation products, Sentinel-1 surface soil-moisture retrievals,

the MCD12Q1 annual land-cover layer and irrigation records. The 1 km analysis grid is suited to governorate-scale trends; Landsat-derived LST and surface reflectance, Sentinel-2 vegetation indices at 10–30 m, or statistical downscaling of the MODIS LST fields [93] would extend the analysis to the sub-pixel heterogeneity of the urbanising Tihama and of the fragmented Sarawat terraces. The 21-year record exceeds the minimum generally recommended for robust Mann–Kendall inference [35]; set against the multi-decadal variability of regional precipitation [45,49], the trends characterise the 2003–2023 climatic state.

The robustness of the main results was examined at each analytical stage. The pixel-level correlations are used descriptively because spatial autocorrelation reduces the effective number of independent pixels below the nominal counts; effective-sample-size corrections such as those of Clifford et al. [73] and Dutilleul et al. [74], or spatially blocked resampling [94], would support an inferential treatment. The cluster analysis is based on 17 governorates, and its most robust feature is the highland–lowland division (Section 3.3). Governorate boundaries follow administrative rather than physiographic limits, so that units such as Ar Rayth contain heterogeneous terrain, and the Jizan unit of the GADM 4.1 layer, which is dominated by its inland block (Section 2.1), is not representative of Jizan City. The white-sky sensitivity analysis (Section 2.2.3) confirms that the significant albedo trends and the cluster partition are unchanged when white-sky albedo is used. Finally, the tercile classes are defined relative to the 2003–2023 distribution of the region (Section 2.6); calibration against field indicators of degradation would give them an absolute interpretation.

The bivariate tercile classification of Section 2.6, while well suited to revealing the joint spatial structure of the four variables, treats each pixel-year independently and does not exploit the temporal sequencing of joint-class transitions. A continuous-time analysis of class-transition probabilities, or of pixel-level trajectories through the joint-class state space, would complement the present categorical approach. Likewise, the PCA–Ward characterisation operates on a single trend statistic per governorate–variable combination and could be extended to a fully temporal framework, for instance through functional principal component analysis or dynamic-time-warping clustering of the per-governorate annual series, to capture the timing and asynchrony of the surface-property transitions identified here.

5. Conclusions

This study has provided the first integrated multi-variable trend characterisation of the surface-energy-balance signature of land degradation and land recovery across the seventeen governorates of the Jizan region for 2003–2023, drawing on four MODIS-derived variables (LST_{Day}, LST_{Night}, NDVI and shortwave black-sky albedo) and a combined statistical framework of Theil–Sen and Mann–Kendall trend estimation, bivariate tercile classification, pixel-level correlation analysis and PCA–Ward hierarchical clustering at the administrative scale.

The analysis shows that no governorate exhibits the absolute Charney–Otterman-related surface signature of daytime warming, vegetation decline and surface brightening. Across the region, the four variables co-evolve in a recovery-consistent direction characterised by significant greening in all 17 governorates (marginal in Farasan after adjustment for multiple testing), declining albedo over much of the Tihama–Sarawat transect and a marked day–night thermal asymmetry in which significant nighttime warming in 16 of 17 governorates coexists with daytime stability or cooling. The strength of this recovery differs between regimes: it is strongest on the southeastern escarpment (Al Aridah and Al Harth) and weakest in the cluster formed by Ad Darb, Ar Rayth, Farasan and Jizan, where greening is slow and daytime LST and albedo have remained nearly stable. This cluster lies

closest to the degradation signature in relative terms, but it represents lagging recovery rather than active degradation. The four-regime classification should be read together with its stability assessment. The block-bootstrap analysis showed that the broader division between the highland and escarpment governorates and the lowland, northern and insular governorates is the most stable feature of the partition. The finer four-cluster structure, although reproduced under alternative clustering algorithms and standardisations, was recovered in only a minority of bootstrap replicates; it therefore describes gradations in the strength of the recovery signal rather than sharply separated classes.

The study contributes to the literature on dryland systems under global change in several respects. The documented spatial footprint of dryland greening is extended to the southwestern Saudi Arabian sector, where the signal is shown to be structured along physiographic and land-use gradients rather than uniformly distributed [9–11]. Diurnal LST asymmetry is shown to be a consistent regional surface-property diagnostic that reproduces the global day–night warming pattern at the governorate scale [37–39] and that, in combination with independent soil-moisture, irrigation and land-cover data, may help to separate moisture-subsidised greening from greening sustained by rainfall and land management. A transferable analytical framework is introduced that combines pooled-threshold bivariate tercile classification with PCA–Ward clustering of standardised Theil–Sen trend vectors, producing administratively aligned, physically interpretable trend signatures without recourse to pre-specified threshold rules, and that is directly portable to other arid and semi-arid administrative units across the Arabian Peninsula and beyond; its outputs are most informative when relative signatures are reported together with absolute trends and when the stability of the partition is assessed.

For regional policy, the weak recovery of the Cluster 4 governorates identifies them as the first targets for diagnostic field and land-cover assessment and, where warranted, for restoration under the environmental commitments of the Saudi Vision 2030 framework and the Saudi Green Initiative, while the dominant recovery-consistent signal elsewhere argues for redirecting monitoring resources towards the trajectories of irrigated agriculture, groundwater abstraction and urban expansion, whose contributions to the observed greening and diurnal-range compression have yet to be established with independent hydrological and land-use evidence. As an implementation tool, the governorate-scale clustering framework can serve as a routinely updatable instrument for desertification, land-degradation-neutrality and afforestation reporting, providing decision-makers with a spatially explicit, low-cost satellite diagnostic that distinguishes governorates with strong surface-energy-balance recovery from those in which recovery is lagging, and that aligns with the administrative units through which regional environmental policy is designed and delivered. The trends reported here characterise the direction, magnitude and spatial organisation of surface-energy-balance change; the processes behind them are a matter for independent evidence rather than for the satellite record alone.

Author Contributions: Conceptualization, I.M.H. and K.K.-W.; methodology, I.M.H., K.K.-W. and Y.M.Y.; software, I.M.H.; validation, I.M.H., K.K.-W., M.Z. and Y.M.Y.; formal analysis, I.M.H., A.A. and S.A.-A.; investigation, I.M.H., K.K.-W., A.A., S.A.-A. and J.I.A.; resources, K.K.-W., M.Z. and Y.M.Y.; data curation, I.M.H. and S.A.-A.; writing—original draft preparation, I.M.H.; writing—review and editing, I.M.H., K.K.-W., A.A., M.Z., S.A.-A., J.I.A. and Y.M.Y.; visualization, I.M.H. and S.A.-A.; supervision, K.K.-W., M.Z. and Y.M.Y.; project administration, K.K.-W. and Y.M.Y.; funding acquisition, K.K.-W. and M.Z. All authors have read and agreed to the published version of the manuscript.

Funding: This research was funded by the Princess Nourah bint Abdulrahman University Researchers Supporting Project number (PNURSP2026R668), Princess Nourah bint Abdulrahman University, Riyadh, Saudi Arabia.

Institutional Review Board Statement: Not applicable.

Informed Consent Statement: Not applicable.

Data Availability Statement: The MODIS products analysed in this study (MOD11A2, MOD13A2 and MCD43A3) are publicly available from the NASA Land Processes Distributed Active Archive Center.

Acknowledgments: The authors extend their appreciation to the Princess Nourah bint Abdulrahman University Researchers Supporting Project number (PNURSP2026R668), Princess Nourah bint Abdulrahman University, Riyadh, Saudi Arabia.

Conflicts of Interest: The authors declare no conflicts of interest. The funders had no role in the design of the study; in the collection, analyses, or interpretation of data; in the writing of the manuscript; or in the decision to publish the results.

Abbreviations

The following abbreviations are used in this manuscript:

ARI	Adjusted Rand index
BRDF	Bidirectional reflectance distribution function
DJF, MAM, JJA, SON	Winter, spring, summer and autumn seasons (December–February, March–May, June–August, September–November)
FDR	False discovery rate
LST	Land surface temperature
LST_{Day}, LST_{Night}	Daytime and nighttime land surface temperature
MK	Mann–Kendall test
MODIS	Moderate Resolution Imaging Spectroradiometer
NDVI	Normalised Difference Vegetation Index
PC	Principal component
PCA	Principal component analysis
QA/QC	Quality assurance/quality control
SVD	Singular value decomposition

Appendix A

Tables A1 and A2 report, for each governorate and variable, the Theil–Sen slope, the unadjusted Mann–Kendall p-value (p), the p-value of the variance-corrected test with the correction factor bounded below at 1 (p^*) and the Benjamini–Hochberg FDR-adjusted value (q) computed within each variable. The symbol † marks governorates in which the original and variance-corrected tests disagree at the 5% level.

Table A1. Trend statistics of daytime and nighttime LST for the 17 governorates, 2003–2023.

Governorate	LST_{Day} (°C yr^{-1})				LST_{Night} (°C yr^{-1})			
	Slope	p	p^*	q	Slope	p	p^*	q
Abu Arish	−0.060	0.012	0.012	0.068	+0.077	<0.001	<0.001	<0.001
Ad Dair	−0.023	0.415	0.415	0.504	+0.039	0.012	0.012	0.014
Ad Darb	−0.022	0.608	0.608	0.689	+0.052	<0.001	<0.001	<0.001
Ahad Al Masarihah	−0.024	0.194	0.194	0.275	+0.066	<0.001	<0.001	0.001
Al Aridah	−0.059	0.001	0.001	0.007	+0.033	0.006	0.006	0.008
Al Aydabi	−0.040	0.075	0.075	0.181	+0.030	0.010	0.010	0.012

Table A1. *Cont.*

Governorate	LST_{Day} (°C yr^{-1})				LST_{Night} (°C yr^{-1})			
	Slope	*p*	*p**	*q*	Slope	*p*	*p**	*q*
Al Harth	−0.099	<0.001	<0.001	0.007	+0.030	0.027	0.027	0.029
Ar Rayth	−0.003	0.880	0.880	0.935	+0.038	0.004	0.004	0.006
At Tuwal	−0.029	0.020	0.020	0.068	+0.064	0.001	0.001	0.002
Baysh	−0.030	0.156	0.156	0.241	+0.069	<0.001	<0.001	<0.001
Damad	−0.046	0.057	0.057	0.162	+0.070	<0.001	<0.001	0.001
Farasan	−0.011	0.349	0.349	0.457	+0.068	<0.001	<0.001	<0.001
Fayfa	−0.053	0.017	0.017	0.068	+0.021	0.057	0.057	0.057
Harub	−0.032	0.110	0.110	0.186	+0.032	0.006	0.006	0.008
Jizan	0.000	1.000	1.000	1.000	+0.045	0.001	0.001	0.002
Sabya	−0.039	0.097	0.097	0.183	+0.059	0.001	0.001	0.001
Samtah	−0.040	0.085	0.085	0.181	+0.059	0.001	0.001	0.001

Slopes in °C yr^{-1}. *p* is the unadjusted Mann–Kendall *p*-value shown in Figures 3b, 4b, 5b and 6b; *p**, variance-corrected *p*-value (Hamed–Rao correction, factor bounded below at 1); *q*, Benjamini–Hochberg FDR-adjusted *p*-value within the variable. The original and variance-corrected tests agree at the 5% level for every LST series, so the symbol †used in Table A2 does not occur in this table. Trends flagged as significant in the figures with $p = 0.050$ have $p = 0.0497$ before rounding.

Table A2. Trend statistics of NDVI and black-sky albedo for the 17 governorates, 2003–2023.

Governorate	NDVI (10^{-3} yr^{-1})				Albedo (10^{-4} yr^{-1})			
	Slope	*p*	*p**	*q*	Slope	*p*	*p**	*q*
Abu Arish	+2.9	<0.001	0.003	0.001	−10.8	0.002	0.020	0.013
Ad Dair	+4.0	0.001	0.001	0.002	−4.5	0.012	0.012	0.041
Ad Darb	+1.0	0.014	0.014	0.015	−2.2	0.139	0.139	0.157
Ahad Al Masarihah	+1.8	0.012	0.058 †	0.014	−9.0	0.050	0.208 †	0.070
Al Aridah	+5.8	<0.001	0.002	0.001	−11.2	0.002	0.053 †	0.013
Al Aydabi	+4.9	<0.001	<0.001	0.001	−4.9	0.020	0.020	0.049
Al Harth	+7.6	<0.001	<0.001	<0.001	−15.8	0.001	0.019	0.009
Ar Rayth	+2.8	0.005	0.052 †	0.007	−3.1	0.050	0.050	0.070
At Tuwal	+2.1	0.001	0.008	0.001	−10.6	0.027	0.129 †	0.052
Baysh	+1.6	0.007	0.042	0.009	−7.3	0.027	0.149 †	0.052
Damad	+1.7	0.007	0.007	0.009	−5.5	0.097	0.184	0.117
Farasan	+0.3	0.050	0.050	0.050	−0.2	0.833	0.833	0.833
Fayfa	+6.7	<0.001	<0.001	0.001	−2.4	0.097	0.097	0.117
Harub	+6.0	0.001	0.029	0.002	−5.2	0.017	0.108 †	0.048
Jizan	+1.6	0.002	0.022	0.002	−3.2	0.264	0.383	0.280
Sabya	+1.8	0.002	0.010	0.002	−6.1	0.043	0.113 †	0.070
Samtah	+2.4	0.001	0.001	0.002	−9.0	0.009	0.045	0.037

Slopes in 10^{-3} NDVI units yr^{-1} and 10^{-4} albedo units yr^{-1}. *p* is the unadjusted Mann–Kendall *p*-value shown in Figures 3b, 4b, 5b and 6b; *p**, variance-corrected *p*-value (Hamed–Rao correction, factor bounded below at 1); *q*, Benjamini–Hochberg FDR-adjusted *p*-value within the variable; †, original and corrected tests disagree at the 5% level. Trends flagged as significant in the figures with $p = 0.050$ have $p = 0.0497$ before rounding.

References

1. Reynolds, J.F.; Stafford Smith, D.M.; Lambin, E.F.; Turner, B.L., II; Mortimore, M.; Batterbury, S.P.J.; Downing, T.E.; Dowlatabadi, H.; Fernández, R.J.; Herrick, J.E.; et al. Global desertification: Building a science for dryland development. *Science* **2007**, *316*, 847–851. [CrossRef] [PubMed]
2. IPCC. *Climate Change and Land: An IPCC Special Report on Climate Change, Desertification, Land Degradation, Sustainable Land Management, Food Security, and Greenhouse Gas Fluxes in Terrestrial Ecosystems*; Shukla, P.R., Skea, J., Calvo Buendia, E., Masson-Delmotte, V., Pörtner, H.-O., Roberts, D.C., Zhai, P., Slade, R., Connors, S., van Diemen, R., et al., Eds.; Intergovernmental Panel on Climate Change: Geneva, Switzerland, 2019.

3. Bestelmeyer, B.T.; Okin, G.S.; Duniway, M.C.; Archer, S.R.; Sayre, N.F.; Williamson, J.C.; Herrick, J.E. Desertification, land use, and the transformation of global drylands. *Front. Ecol. Environ.* **2015**, *13*, 28–36. [CrossRef]
4. Verstraete, M.M.; Scholes, R.J.; Stafford Smith, M. Climate and desertification: Looking at an old problem through new lenses. *Front. Ecol. Environ.* **2009**, *7*, 421–428. [CrossRef]
5. Otterman, J. Baring high-albedo soils by overgrazing: A hypothesized desertification mechanism. *Science* **1974**, *186*, 531–533. [CrossRef] [PubMed]
6. Charney, J.G. Dynamics of deserts and drought in the Sahel. *Q. J. R. Meteorol. Soc.* **1975**, *101*, 193–202. [CrossRef]
7. Karnieli, A.; Agam, N.; Pinker, R.T.; Anderson, M.; Imhoff, M.L.; Gutman, G.G.; Panov, N.; Goldberg, A. Use of NDVI and land surface temperature for drought assessment: Merits and limitations. *J. Clim.* **2010**, *23*, 618–633. [CrossRef]
8. Donohue, R.J.; Roderick, M.L.; McVicar, T.R.; Farquhar, G.D. Impact of CO_2 fertilization on maximum foliage cover across the globe's warm, arid environments. *Geophys. Res. Lett.* **2013**, *40*, 3031–3035. [CrossRef]
9. Fensholt, R.; Langanke, T.; Rasmussen, K.; Reenberg, A.; Prince, S.D.; Tucker, C.; Scholes, R.J.; Le, Q.B.; Bondeau, A.; Eastman, R.; et al. Greenness in semi-arid areas across the globe 1981–2007—An Earth Observing Satellite based analysis of trends and drivers. *Remote Sens. Environ.* **2012**, *121*, 144–158. [CrossRef]
10. Zhu, Z.; Piao, S.; Myneni, R.B.; Huang, M.; Zeng, Z.; Canadell, J.G.; Ciais, P.; Sitch, S.; Friedlingstein, P.; Arneth, A.; et al. Greening of the Earth and its drivers. *Nat. Clim. Change* **2016**, *6*, 791–795. [CrossRef]
11. Piao, S.; Wang, X.; Park, T.; Chen, C.; Lian, X.; He, Y.; Bjerke, J.W.; Chen, A.; Ciais, P.; Tømmervik, H.; et al. Characteristics, drivers and feedbacks of global greening. *Nat. Rev. Earth Environ.* **2020**, *1*, 14–27. [CrossRef]
12. Chen, C.; Park, T.; Wang, X.; Piao, S.; Xu, B.; Chaturvedi, R.K.; Fuchs, R.; Brovkin, V.; Ciais, P.; Fensholt, R.; et al. China and India lead in greening of the world through land-use management. *Nat. Sustain.* **2019**, *2*, 122–129. [CrossRef] [PubMed]
13. Abbas, W.; Hamdi, I. Satellite-based discrimination of urban dynamics-induced local bias from day/night temperature trends across the Nile Delta, Egypt: A basis for climate change impacts assessment. *Sustainability* **2022**, *14*, 14510. [CrossRef]
14. Alasgah, A.A.; Ahmad, I.; Dar, M.A.; Youssef, Y.M.; Zelenakova, M.; Sisay, M.; Zewdu, G.S.; Heiba, Y. Integrating GIS–Fuzzy logic framework and remotely sensed climate data for drought vulnerability assessment across Africa. *Environ. Monit. Assess.* **2025**, *197*, 1110. [CrossRef] [PubMed]
15. Justice, C.O.; Townshend, J.R.G.; Vermote, E.F.; Masuoka, E.; Wolfe, R.E.; Saleous, N.; Roy, D.P.; Morisette, J.T. An overview of MODIS Land data processing and product status. *Remote Sens. Environ.* **2002**, *83*, 3–15. [CrossRef]
16. Wan, Z.; Dozier, J. A generalized split-window algorithm for retrieving land-surface temperature from space. *IEEE Trans. Geosci. Remote Sens.* **1996**, *34*, 892–905. [CrossRef]
17. Wan, Z. New refinements and validation of the Collection-6 MODIS land-surface temperature/emissivity product. *Remote Sens. Environ.* **2014**, *140*, 36–45. [CrossRef]
18. Tucker, C.J. Red and photographic infrared linear combinations for monitoring vegetation. *Remote Sens. Environ.* **1979**, *8*, 127–150. [CrossRef]
19. Huete, A.; Didan, K.; Miura, T.; Rodriguez, E.P.; Gao, X.; Ferreira, L.G. Overview of the radiometric and biophysical performance of the MODIS vegetation indices. *Remote Sens. Environ.* **2002**, *83*, 195–213. [CrossRef]
20. Didan, K. *MODIS/Terra Vegetation Indices 16-Day L3 Global 1km SIN Grid V061 [Dataset]*; NASA Land Processes Distributed Active Archive Center: Sioux Falls, SD, USA, 2021. [CrossRef]
21. Pettorelli, N.; Vik, J.O.; Mysterud, A.; Gaillard, J.-M.; Tucker, C.J.; Stenseth, N.C. Using the satellite-derived NDVI to assess ecological responses to environmental change. *Trends Ecol. Evol.* **2005**, *20*, 503–510. [CrossRef] [PubMed]
22. Lucht, W.; Schaaf, C.B.; Strahler, A.H. An algorithm for the retrieval of albedo from space using semiempirical BRDF models. *IEEE Trans. Geosci. Remote Sens.* **2000**, *38*, 977–998. [CrossRef]
23. Schaaf, C.B.; Gao, F.; Strahler, A.H.; Lucht, W.; Li, X.; Tsang, T.; Strugnell, N.C.; Zhang, X.; Jin, Y.; Muller, J.-P.; et al. First operational BRDF, albedo nadir reflectance products from MODIS. *Remote Sens. Environ.* **2002**, *83*, 135–148. [CrossRef]
24. Schaaf, C.; Wang, Z. *MODIS/Terra+Aqua BRDF/Albedo Daily L3 Global-500m V061 [Dataset]*; NASA Land Processes Distributed Active Archive Center: Sioux Falls, SD, USA, 2021. [CrossRef]
25. Bento, V.A.; Gouveia, C.M.; DaCamara, C.C.; Trigo, I.F. A climatological assessment of drought impact on vegetation health index. *Agric. For. Meteorol.* **2018**, *259*, 286–295. [CrossRef]
26. Julien, Y.; Sobrino, J.A. The Yearly Land Cover Dynamics (YLCD) method: An analysis of global vegetation from NDVI and LST parameters. *Remote Sens. Environ.* **2009**, *113*, 329–334. [CrossRef]
27. Sun, D.; Kafatos, M. Note on the NDVI-LST relationship and the use of temperature-related drought indices over North America. *Geophys. Res. Lett.* **2007**, *34*, L24406. [CrossRef]
28. Mu, Q.; Zhao, M.; Kimball, J.S.; McDowell, N.G.; Running, S.W. A remotely sensed global terrestrial drought severity index. *Bull. Am. Meteorol. Soc.* **2013**, *94*, 83–98. [CrossRef]
29. Bonan, G.B. Forests and climate change: Forcings, feedbacks, and the climate benefits of forests. *Science* **2008**, *320*, 1444–1449. [CrossRef] [PubMed]

30. Mildrexler, D.J.; Zhao, M.; Running, S.W. A global comparison between station air temperatures and MODIS land surface temperatures reveals the cooling role of forests. *J. Geophys. Res. Biogeosci.* **2011**, *116*, G03025. [CrossRef]
31. Theil, H. A rank-invariant method of linear and polynomial regression analysis, I, II and III. *Proc. K. Ned. Akad. Wet. A* **1950**, *53*, 386–392, 521–525, 1397–1412.
32. Sen, P.K. Estimates of the regression coefficient based on Kendall's tau. *J. Am. Stat. Assoc.* **1968**, *63*, 1379–1389. [CrossRef]
33. Mann, H.B. Nonparametric tests against trend. *Econometrica* **1945**, *13*, 245–259. [CrossRef]
34. Kendall, M.G. *Rank Correlation Methods*, 4th ed.; Charles Griffin: London, UK, 1975.
35. Hamed, K.H.; Rao, A.R. A modified Mann-Kendall trend test for autocorrelated data. *J. Hydrol.* **1998**, *204*, 182–196. [CrossRef]
36. Dai, A.; Trenberth, K.E.; Karl, T.R. Effects of clouds, soil moisture, precipitation, and water vapor on diurnal temperature range. *J. Clim.* **1999**, *12*, 2451–2473. [CrossRef]
37. Davy, R.; Esau, I.; Chernokulsky, A.; Outten, S.; Zilitinkevich, S. Diurnal asymmetry to the observed global warming. *Int. J. Climatol.* **2017**, *37*, 79–93. [CrossRef]
38. Karl, T.R.; Kukla, G.; Razuvayev, V.N.; Changery, M.J.; Quayle, R.G.; Heim, R.R., Jr.; Easterling, D.R.; Fu, C.B. Global warming: Evidence for asymmetric diurnal temperature change. *Geophys. Res. Lett.* **1991**, *18*, 2253–2256. [CrossRef]
39. Vose, R.S.; Easterling, D.R.; Gleason, B. Maximum and minimum temperature trends for the globe: An update through 2004. *Geophys. Res. Lett.* **2005**, *32*, L23822. [CrossRef]
40. Seneviratne, S.I.; Corti, T.; Davin, E.L.; Hirschi, M.; Jaeger, E.B.; Lehner, I.; Orlowsky, B.; Teuling, A.J. Investigating soil moisture–climate interactions in a changing climate: A review. *Earth-Sci. Rev.* **2010**, *99*, 125–161. [CrossRef]
41. Hereher, M.E. Assessment of seasonal warming trends at the Nile Delta: A paradigm for human-induced climate change. *Environ. Monit. Assess.* **2024**, *196*, 20. [CrossRef] [PubMed]
42. Youssef, Y.M.; Đurin, B.; Alturki, A.A.; Šrajbek, M.; Hamdi, I.M. Two decades of optical and thermal variability in Lake Nasser: A multi-variable MODIS assessment on a 5 km analysis grid (2005–2025). *Water* **2026**, *18*, 2213. [CrossRef]
43. Almazroui, M. Rainfall trends and extremes in Saudi Arabia in recent decades. *Atmosphere* **2020**, *11*, 964. [CrossRef]
44. AlSarmi, S.; Washington, R. Recent observed climate change over the Arabian Peninsula. *J. Geophys. Res. Atmos.* **2011**, *116*, D11109. [CrossRef]
45. Almazroui, M.; Islam, M.N.; Athar, H.; Jones, P.D.; Rahman, M.A. Recent climate change in the Arabian Peninsula: Annual rainfall and temperature analysis of Saudi Arabia for 1978–2009. *Int. J. Climatol.* **2012**, *32*, 953–966. [CrossRef]
46. Almazroui, M.; Islam, M.N.; Dambul, R.; Jones, P.D. Trends of temperature extremes in Saudi Arabia. *Int. J. Climatol.* **2014**, *34*, 808–826. [CrossRef]
47. AlSarmi, S.H.; Washington, R. Changes in climate extremes in the Arabian Peninsula: Analysis of daily data. *Int. J. Climatol.* **2014**, *34*, 1329–1345. [CrossRef]
48. Athar, H. Trends in observed extreme climate indices in Saudi Arabia during 1979–2008. *Int. J. Climatol.* **2014**, *34*, 1561–1574. [CrossRef]
49. Tarawneh, Q.Y.; Chowdhury, S. Trends of climate change in Saudi Arabia: Implications on water resources. *Climate* **2018**, *6*, 8. [CrossRef]
50. Alzahrani, A.A.; Hamdi, I.M.; Selín, J.; Al-Hosan, A.M.; Dobransky, M.; Aboulola, O.I.; Youssef, Y.M. Hybrid hydroinformatic assessment of groundwater-storage depletion in Saudi Arabia (2002–2024): Integrating GRACE/GRACE-FO gravimetry, land-surface modeling, and dependence-aware machine learning. *Front. Environ. Sci.* **2026**, *14*, 1975725. [CrossRef]
51. Hereher, M.E. Recent trends of temperature and precipitation proxies in Saudi Arabia: Implications for climate change. *Arab. J. Geosci.* **2016**, *9*, 631. [CrossRef]
52. Assiri, M.E.; Ali, M.A.; Alamri, L.; Siddiqui, M.H.; Ghulam, A.S.; Shahid, S. Spatio-temporal dynamics of vegetation and land surface temperature in Saudi Arabia: Impacts of climate change on agricultural sites from 2010 to 2023. *Int. J. Climatol.* **2025**, *45*, e8781. [CrossRef]
53. Hamdi, I.; Fawzy, M.; Zelenakova, M.; Abbas, W. Heat island dynamics and heat stress implications on the population of El-Mansourah conurbation, Egypt: Temporal and proposed solutions using MODIS imagery and ENVI-met simulation. *Geomat. Nat. Hazards Risk* **2024**, *15*, 2291328. [CrossRef]
54. Hauke, J.; Kossowski, T. Comparison of values of Pearson's and Spearman's correlation coefficients on the same sets of data. *Quaest. Geogr.* **2011**, *30*, 87–93. [CrossRef]
55. Bawadekji, A.; Tonbol, K.; Ghazouani, N.; Becheikh, N.; Shaltout, M. Recent atmospheric changes and future projections along the Saudi Arabian Red Sea Coast. *Sci. Rep.* **2022**, *12*, 160. [CrossRef] [PubMed]
56. El-Hamid, H.T.A.; Hafiz, M.A.; Wenlong, W.; Qiaomin, L. Detection of environmental degradation in Jazan Region on the Red Sea, KSA, using mathematical treatments of remote sensing data. *Remote Sens. Earth Syst. Sci.* **2019**, *2*, 183–196. [CrossRef]
57. Alharbi, O.A.; Rangel-Buitrago, N. Landscape degradation in the Jazan coastal desert: Understanding the impact of human activities. *Mar. Pollut. Bull.* **2023**, *190*, 114874. [CrossRef] [PubMed]

58. Hasan, S.S.; Alharbi, O.A.; Alqurashi, A.F.; Fahil, A.S. Assessment of desertification dynamics in arid coastal areas by integrating remote sensing data and statistical techniques. *Sustainability* **2024**, *16*, 4527. [CrossRef]
59. GADM. *GADM Database of Global Administrative Areas, Version 4.1*; GADM: Davis, CA, USA, 2022. Available online: https://gadm.org/data.html (accessed on 22 September 2026).
60. Gorelick, N.; Hancher, M.; Dixon, M.; Ilyushchenko, S.; Thau, D.; Moore, R. Google Earth Engine: Planetary-scale geospatial analysis for everyone. *Remote Sens. Environ.* **2017**, *202*, 18–27. [CrossRef]
61. Wan, Z.; Hook, S.; Hulley, G. *MODIS/Terra Land Surface Temperature/Emissivity 8-Day L3 Global 1 km SIN Grid V061 [Dataset]*; NASA Land Processes Distributed Active Archive Center: Sioux Falls, SD, USA, 2021. [CrossRef]
62. Gillies, S. *the Rasterio Contributors. Rasterio: Geospatial Raster I/O for Python Programmers, Version 1.5.2; Mapbox*; Mapbox: San Francisco, CA, USA, 2013. Available online: https://rasterio.readthedocs.io (accessed on 22 September 2026).
63. Eisa, M.; Youssef, Y.M.; Aboulola, O.I.; Aldohan, A.; Dąbrowska, D.; Hamdi, I.M. Silent inconsistencies at the aggregation stage of Earth observation pipelines: An internal-consistency audit of zonal statistics for Local Climate Zone–based land surface temperature analysis. *Front. Environ. Sci.* **2026**, *14*, 1971523. [CrossRef]
64. Wilcox, R.R. *Fundamentals of Modern Statistical Methods: Substantially Improving Power and Accuracy*, 2nd ed.; Springer: New York, NY, USA, 2010. [CrossRef]
65. Hussain, M.; Mahmud, I. pyMannKendall: A Python package for non parametric Mann Kendall family of trend tests. *J. Open Source Softw.* **2019**, *4*, 1556. [CrossRef]
66. Benjamini, Y.; Hochberg, Y. Controlling the false discovery rate: A practical and powerful approach to multiple testing. *J. R. Stat. Soc. Ser. B Methodol.* **1995**, *57*, 289–300. [CrossRef]
67. Wilks, D.S. "The stippling shows statistically significant grid points": How research results are routinely overstated and overinterpreted, and what to do about it. *Bull. Am. Meteorol. Soc.* **2016**, *97*, 2263–2273. [CrossRef]
68. Brewer, C.A. Color use guidelines for mapping and visualization. In *Visualization in Modern Cartography*; MacEachren, A.M., Taylor, D.R.F., Eds.; Elsevier: Oxford, UK, 1994; pp. 123–147.
69. Pearson, K. Note on regression and inheritance in the case of two parents. *Proc. R. Soc. Lond.* **1895**, *58*, 240–242. [CrossRef]
70. Spearman, C. The proof and measurement of association between two things. *Am. J. Psychol.* **1904**, *15*, 72–101. [CrossRef] [PubMed]
71. Kendall, M.G. A new measure of rank correlation. *Biometrika* **1938**, *30*, 81–93. [CrossRef]
72. Carr, D.B.; Littlefield, R.J.; Nicholson, W.L.; Littlefield, J.S. Scatterplot matrix techniques for large N. *J. Am. Stat. Assoc.* **1987**, *82*, 424–436. [CrossRef]
73. Clifford, P.; Richardson, S.; Hémon, D. Assessing the significance of the correlation between two spatial processes. *Biometrics* **1989**, *45*, 123–134. [CrossRef]
74. Dutilleul, P.; Clifford, P.; Richardson, S.; Hemon, D. Modifying the t test for assessing the correlation between two spatial processes. *Biometrics* **1993**, *49*, 305–314. [CrossRef]
75. Jolliffe, I.T.; Cadima, J. Principal component analysis: A review and recent developments. *Philos. Trans. R. Soc. A* **2016**, *374*, 20150202. [CrossRef] [PubMed]
76. Murtagh, F.; Legendre, P. Ward's hierarchical agglomerative clustering method: Which algorithms implement Ward's criterion? *J. Classif.* **2014**, *31*, 274–295. [CrossRef]
77. Jolliffe, I.T. *Principal Component Analysis*, 2nd ed.; Springer: New York, NY, USA, 2002. [CrossRef]
78. Ward, J.H., Jr. Hierarchical grouping to optimize an objective function. *J. Am. Stat. Assoc.* **1963**, *58*, 236–244. [CrossRef]
79. Rousseeuw, P.J. Silhouettes: A graphical aid to the interpretation and validation of cluster analysis. *J. Comput. Appl. Math.* **1987**, *20*, 53–65. [CrossRef]
80. Kaufman, L.; Rousseeuw, P.J. *Finding Groups in Data: An Introduction to Cluster Analysis*; John Wiley & Sons: New York, NY, USA, 1990. [CrossRef]
81. Hubert, L.; Arabie, P. Comparing partitions. *J. Classif.* **1985**, *2*, 193–218. [CrossRef]
82. Hennig, C. Cluster-wise assessment of cluster stability. *Comput. Stat. Data Anal.* **2007**, *52*, 258–271. [CrossRef]
83. Cohen, J. *Statistical Power Analysis for the Behavioral Sciences*, 2nd ed.; Lawrence Erlbaum Associates: Hillsdale, NJ, USA, 1988.
84. Jordahl, K.; Van den Bossche, J.; Fleischmann, M.; Wasserman, J.; McBride, J.; Gerard, J.; Tratner, J.; Perry, M.; Garcia Badaracco, A.; Farmer, C.; et al. *Geopandas/Geopandas*, v0.8.1; Zenodo: Geneva, Switzerland, 2020. [CrossRef]
85. Harris, C.R.; Millman, K.J.; van der Walt, S.J.; Gommers, R.; Virtanen, P.; Cournapeau, D.; Wieser, E.; Taylor, J.; Berg, S.; Smith, N.J.; et al. Array programming with NumPy. *Nature* **2020**, *585*, 357–362. [CrossRef] [PubMed]
86. Virtanen, P.; Gommers, R.; Oliphant, T.E.; Haberland, M.; Reddy, T.; Cournapeau, D.; Burovski, E.; Peterson, P.; Weckesser, W.; Bright, J.; et al. SciPy 1.0: Fundamental algorithms for scientific computing in Python. *Nat. Methods* **2020**, *17*, 261–272. [CrossRef] [PubMed]
87. Hunter, J.D. Matplotlib: A 2D graphics environment. *Comput. Sci. Eng.* **2007**, *9*, 90–95. [CrossRef]

88. Pedregosa, F.; Varoquaux, G.; Gramfort, A.; Michel, V.; Thirion, B.; Grisel, O.; Blondel, M.; Prettenhofer, P.; Weiss, R.; Dubourg, V.; et al. Scikit-learn: Machine learning in Python. *J. Mach. Learn. Res.* **2011**, *12*, 2825–2830.
89. Balling, R.C., Jr. The climatic impact of a Sonoran vegetation discontinuity. *Clim. Change* **1988**, *13*, 99–109. [CrossRef]
90. Hamdi, I.M.; Albalawi, E.; Abd Almapoed, E.K.; Abd Elaal, S.R. Mitigating surface industrial heat island effects in arid environments: A machine learning approach to sustainable planning. *Energy Build.* **2026**, *361*, 117449. [CrossRef]
91. Hamdi, I.; Abd Almapoed, E.K.; Abd Elaal, S.R. Assessment of urban heat island effects in industrial areas of Egypt using robust statistical methods. *Remote Sens. Appl. Soc. Environ.* **2025**, *40*, 101777. [CrossRef]
92. AL-Hammad, S.H.; Hamdi, I.M.; Ahmed, A.M.; Youssef, Y.M. Seasonal day–night thermal asymmetry and diurnal temperature range change in a climatically diverse arid region: Insights from per-pixel Theil–Sen and Mann–Kendall analysis of MODIS data (2003–2023). *Phys. Chem. Earth Parts A/B/C* **2026**, *145*, 104921. [CrossRef]
93. Hamdi, I.M. Fine-scale urban heat mapping by machine learning downscaling of MODIS land surface temperature in a hyper-arid megacity. *Sustain. Cities Soc.* **2026**, *150*, 107878. [CrossRef]
94. Alturki, A.A.; Hamdi, I.M.; Rykała, W.; Dąbrowska, D.; Youssef, Y.M.; Fabiańska, M.J. Interpretable ensemble machine learning for statistical emulation of summer $PM_{2.5}$ change in GEOS-CF over the Arabian Peninsula: How far does spatially blocked skill transfer? *Atmosphere* **2026**, *17*, 1035. [CrossRef]

Disclaimer/Publisher's Note: The statements, opinions and data contained in all publications are solely those of the individual author(s) and contributor(s) and not of MDPI and/or the editor(s). MDPI and/or the editor(s) disclaim responsibility for any injury to people or property resulting from any ideas, methods, instructions or products referred to in the content.